Testbeam Studies of Production Modules of the ATLAS Tile Calorimeter

P. Adragna [a] C. Alexa [b] K. Anderson [c] A. Antonaki [d]
A. Arabidze [d] L. Batkova [e] V. Batusov [f] H. P. Beck [g] P. Bednar [e]
E. Bergeaas Kuutmann [h] C. Biscarat [i] G. Blanchot [j] A. Bogush [k]
C. Bohm [h] V. Boldea [b] M. Bosman [j] C. Bromberg [ℓ] J. Budagov [f]
D. Burckhart-Chromek [m] M. Caprini [b] L. Caloba [n] D. Calvet [i]
T. Carli [m] J. Carvalho [o] M. Cascella [a] J. Castelo [p]
M. V. Castillo [p] M. Cavalli-Sforza [j] V. Cavasinni [a]
A. S. Cerqueira [n] C. Clement [h] M. Cobal [m] F. Cogswell [q]
S. Constantinescu [b] D. Costanzo [a] A. Corso-Radu [m] C. Cuenca [p]
D. O. Damazio [n] M. David [r] T. Davidek [s,m,1] K. De [t]
T. Del Prete [a] B. Di Girolamo [m] S. Dita [b] T. Djobava [u]
M. Dobson [m] J. Dolejsi [s] Z. Dolezal [s] A. Dotti [a] R. Downing [q]
I. Efthymiopoulos [m] D. Eriksson [h] D. Errede [q] S. Errede [q]
A. Farbin [c,m] D. Fassouliotis [d] R. Febbraro [i] I. Fedorko [e]
A. Fenyuk [v] C. Ferdi [i] A. Ferrer [p] V. Flaminio [a] D. Francis [m]
E. Fullana [p] S. Gadomski [g] S. Gameiro [m] V. Garde [i]
K. Gellerstedt [h] V. Giakoumopoulou [d] O. Gildemeister [m]
V. Gilewsky [w] N. Giokaris [d] N. Gollub [m] A. Gomes [r]
V. Gonzalez [p] B. Gorini [m] P. Grenier [m,i] P. Gris [i] M. Gruwe [m]
V. Guarino [x] C. Guicheney [i] A. Gupta [c] C. Haeberli [g]
H. Hakobyan [y] M. Haney [q] S. Hellman [h] A. Henriques [m]
E. Higon [p] S. Holmgren [h] M. Hurwitz [c] J. Huston [ℓ] C. Iglesias [j]
A. Isaev [v] I. Jen-La Plante [c] K. Jon-And [h] M. Joos [m] T. Junk [q]
A. Karyukhin [v] A. Kazarov [z] H. Khandanyan [q] J. Khramov [f]
J. Khubua [u,f] S. Kolos [z] I. Korolkov [j] P. Krivkova [s]
Y. Kulchitsky [k,f] Yu. Kurochkin [k] P. Kuzhir [w] T. Le Compte [x]
R. Lefevre [i] G. Lehmann [m] R. Leitner [s] M. Lembesi [d] J. Lesser [h]
J. Li [t] M. Liablin [f] M. Lokajicek [aa] Y. Lomakin [f,2] A. Lupi [a]
C. Maidanchik [n] A. Maio [r] M. Makouski [v] S. Maliukov [f]
A. Manousakis [d] L. Mapelli [m] C. Marques [r] F. Marroquim [n]

ATL-TILECAL-PUB-2009-002
11 March 2009

F. Martin [m,i] E. Mazzoni [a] F. Merritt [c] A. Miagkov [v] R. Miller [ℓ]
I. Minashvili [f] L. Miralles [j] G. Montarou [i] M. Mosidze [u]
A. Myagkov [v] S. Nemecek [aa] M. Nessi [m] L. Nodulman [x]
B. Nordkvist [h] O. Norniella [j] A. Onofre [ab] M. Oreglia [c] D. Pallin [i]
D. Pantea [b] J. Petersen [m] J. Pilcher [c] J. Pina [r] J. Pinhão [o]
F. Podlyski [i] X. Portell [j] J. Poveda [p] L. Pribyl [aa,m] L. E. Price [x]
J. Proudfoot [x] M. Ramstedt [h] R. Richards [ℓ] C. Roda [a]
V. Romanov [f] P. Rosnet [i] P. Roy [i] A. Ruiz [p] V. Rumiantsev [w,2]
N. Russakovich [f] O. Saltó [j] B. Salvachua [p] E. Sanchis [p]
H. Sanders [c] C. Santoni [i] J. Santos [r] J. G. Saraiva [r] F. Sarri [a]
I. Satsunkevitch [k] L.-P. Says [i] G. Schlager [m] J. Schlereth [x]
J. M. Seixas [n] B. Selldèn [h] N. Shalanda [v] P. Shevtsov [w]
M. Shochet [c] J. Silva [r] P. Da Silva [n] V. Simaitis [q] M. Simonyan [y]
A. Sissakian [f] J. Sjölin [h] C. Solans [p] A. Solodkov [v] I. Soloviev [z]
O. Solovyanov [v] M. Sosebee [t] F. Spanò [m] R. Stanek [x]
E. Starchenko [v] P. Starovoitov [w] P. Stavina [e] M. Suk [s] I. Sykora [e]
F. Tang [c] P. Tas [s] R. Teuscher [c] S. Tokar [e] N. Topilin [f] J. Torres [p]
L. Tremblet [m] P. Tsiareshka [f,k] M. Tylmad [h] D. Underwood [x]
G. Unel [m,ac] G. Usai [a] A. Valero [p] S. Valkar [s] J. A. Valls [p]
A. Vartapetian [t] F. Vazeille [i] I. Vichou [q] V. Vinogradov [f]
I. Vivarelli [a] M. Volpi [j] A. White [t] A. Zaitsev [v] A. Zenine [v]
T. Zenis [e]

[a] *Pisa University and INFN, Pisa, Italy*

[b] *Institute of Atomic Physics, Bucharest, Romania*

[c] *University of Chicago, Chicago, Illinois, USA*

[d] *University of Athens, Athens, Greece*

[e] *Comenius University, Bratislava, Slovakia*

[f] *JINR, Dubna, Russia*

[g] *Laboratory for High Energy Physics, University of Bern, Switzerland*

[h] *Stockholm University, Stockholm, Sweden*

[i] *LPC Clermont–Ferrand, Université Blaise Pascal, Clermont-Ferrand, France*

[j] *Institut de Fisica d'Altes Energies, Universitat Autònoma de Barcelona, Barcelona, Spain*

[k] *Institute of Physics, National Academy of Sciences, Minsk, Belarus*

[ℓ] *Michigan State University, East Lansing, Michigan, USA*

[m] *CERN, Geneva, Switzerland*

[n] *COPPE/EE/UFRJ, Rio de Janeiro, Brazil*

[o] *LIP and FCTUC Univ. of Coimbra, Portugal*

[p] *IFIC, Centro Mixto Universidad de Valencia-CSIC, E46100 Burjassot, Valencia, Spain*

[q] *University of Illinois, Urbana–Champaign, Illinois, USA*

[r] *LIP and FCUL Univ. of Lisbon, Portugal*

[s] *Charles University, Faculty of Mathematics and Physics, Prague, Czech Republic*

[t] *University of Texas at Arlington, Arlington, Texas, USA*

[u] *HEPI, Tbilisi State University, Tbilisi, Georgia*

[v] *Institute for High Energy Physics, Protvino, Russia*

[w] *National Centre of Particles and High Energy Physics, Minsk, Belarus*

[x] *Argonne National Laboratory, Argonne, Illinois, USA*

[y] *Yerevan Physics Institute, Yerevan, Armenia*

[z] *Petersburg Nuclear Physics Institute (PNPI), Gatchina, Russia*

[aa] *Institute of Physics, Academy of Sciences of the Czech Republic, Prague, Czech Republic*

[ab] *LIP and Univ. Católica Figueira da Foz, Portugal*

[ac] *University of California, Irvine, CA 92717 USA*

Abstract

We report test beam studies of 11 % of the production ATLAS Tile Calorimeter modules. The modules were equipped with production front-end electronics and all the calibration systems planned for the final detector. The studies used muon, electron and hadron beams ranging in energy from 3 GeV to 350 GeV.

Two independent studies showed that the light yield of the calorimeter was $\sim$ 70 pe/GeV, exceeding the design goal by 40 %. Electron beams provided a calibration of the modules at the electromagnetic energy scale. Over 200 calorimeter cells the variation of the response was 2.4 %. The linearity with energy was also measured. Muon beams provided an intercalibration of the response of all calorimeter cells. The response to muons entering in the ATLAS projective geometry showed an RMS variation of 2.5 % for 91 measurements over a range of rapidities and modules. The mean response to hadrons of fixed energy had an RMS variation of 1.4 % for the modules and projective angles studied. The response to hadrons normalized to incident beam energy showed an 8 % increase between 10 GeV and 350 GeV, fully consistent with expectations for a non-compensating calorimeter. The measured energy resolution for hadrons of $\sigma/E = 52.9\,\%/\sqrt{E} \oplus 5.7\,\%$ was also consistent with expectations.

Other auxiliary studies were made of saturation recovery of the readout system, the time resolution of the calorimeter and the performance of the trigger signals from the calorimeter.

[1] Corresponding author, e-mail address: Tomas.Davidek@cern.ch
[2] Deceased

1 Introduction

The ATLAS experiment at the CERN Large Hadron Collider (LHC) is designed to exploit fully the exciting opportunities for fundamental discoveries at the next high-energy frontier. The proton-proton center of mass energy of 14 TeV, the design luminosity of 10^{34} cm^{-2}s^{-1} and the time between bunch crossings of 25 ns are the basic collider parameters that drove the design of the experiment. The ATLAS detector as built and its expected performance are described in Ref. [1] and its physics program is documented in Ref. [2]. At the present time, the detector is installed and is being commissioned in the underground area at interaction point 1 of the LHC.

Electromagnetic and hadronic calorimeters are indispensable components of a general-purpose hadron collider detector. Jointly they must provide accurate energy and position measurements of electrons, photons, isolated hadrons, jets, and transverse missing energy, as well as helping in particle identification and in muon momentum reconstruction. The electromagnetic (EM) and hadronic compartments of the ATLAS calorimeter system cover the pseudorapidity region $|\eta| < 4.9$. The EM compartments are liquid argon sampling calorimeters, while the detector media of the hadronic calorimeters differ according to the η region. The Tile Calorimeter (TileCal) is a sampling plastic scintillator/iron detector, located in the region $|\eta| < 1.7$; it is divided into three cylindrical sections, referred to as the barrel and extended barrels (EB). Radially, the Tile Calorimeter extends from an inner radius of 2.28 m to an outer radius of 4.25 m. Before reaching TileCal, particles from the collision region first traverse the inner tracking detectors and the barrel or endcap sections of the liquid argon/lead EM calorimeters. [1] The general layout of the ATLAS calorimeter system is shown in Fig. 1. A detailed description of the ATLAS TileCal is given in Ref. [3]. The essential aspects are illustrated in this introduction.

Each of the three TileCal barrels is composed of 64 azimuthal segments, referred to as modules, subtending $\Delta\phi = 2\pi/64 \simeq 0.1$. A schematic drawing of a module is given in Fig. 2.

The TileCal scintillator plates [2] are placed perpendicular to the colliding beam axis, and are radially staggered in depth. The structure is periodic along the beam axis. The tiles are 3 mm thick and the total thickness of the iron plates in one 18 mm period is 14 mm. Two sides of the scintillating tiles are read out by wave-length shifting (WLS) fibers [3] into two separate photomultipliers

[1] For $|\eta| > 1.5$, particles also traverse the liquid argon/copper endcap calorimeter.
[2] Custom-produced by injection molding of polystyrene, doped with 1.5 % PTP and 0.044 % POPOP [4].
[3] Kuraray Y11(200)MSJ double-clad 1 mm diameter fibers.

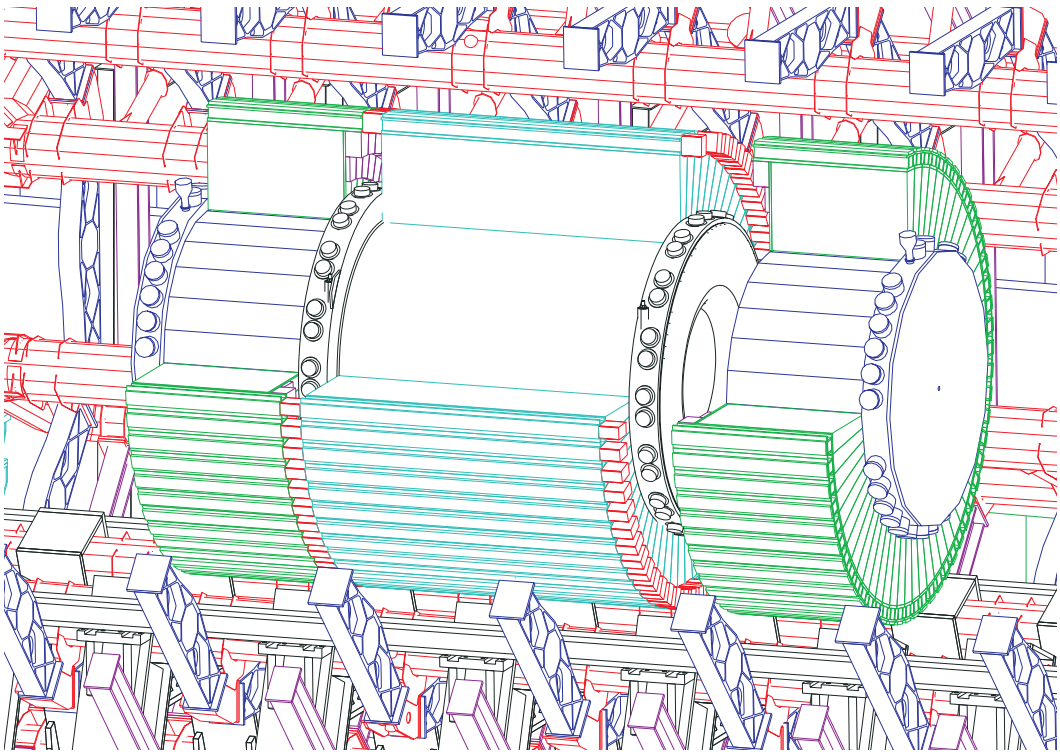

Fig. 1. The Tile Calorimeter in the ATLAS detector. Shown are both the barrel and two extended barrel sections surrounding the electromagnetic calorimeters.

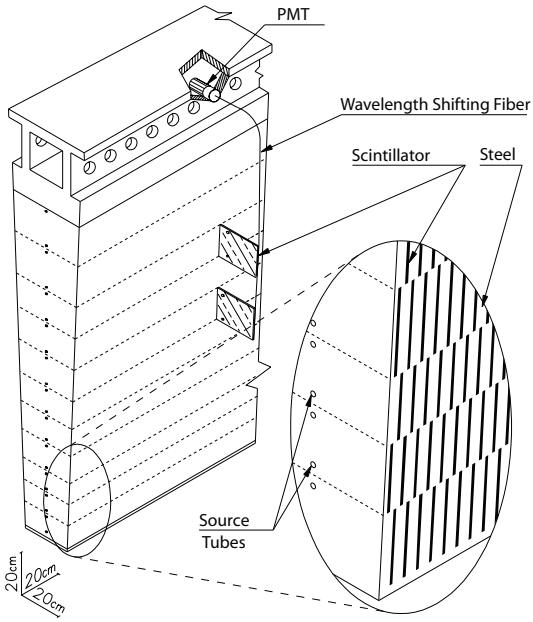

Fig. 2. Mechanical structure of a TileCal module, showing the slots in the iron for scintillating tiles and the method of light collection by WLS fibers to PMTs. The holes for radioactive source tubes that traverse the module parallel to the colliding beams are also shown.

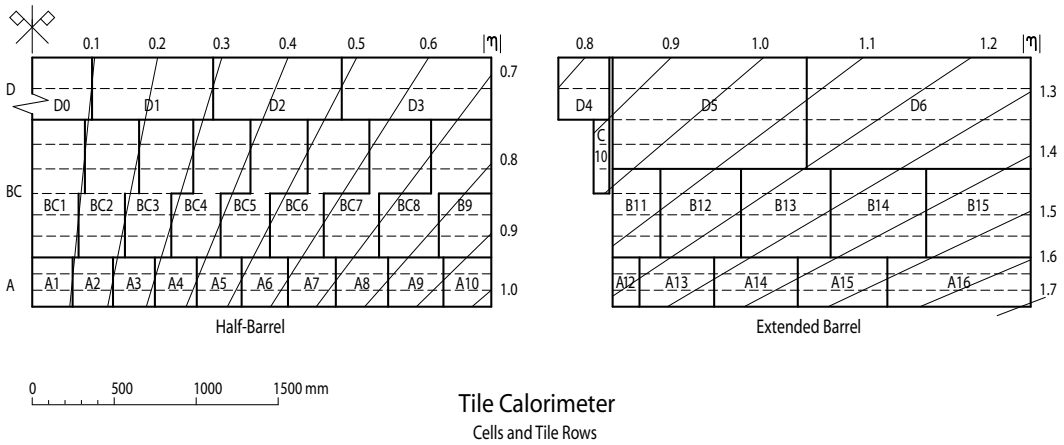

Fig. 3. Cells and tile-rows in the barrel and extended barrel sections of the calorimeter. Horizontal lines delineate the eleven rows of scintillating tiles. Heavy lines show the cell boundaries formed by grouping optical fibers from the tiles for read out by separate photomultipliers. Also shown are lines of fixed pseudorapidity.

(PMTs).[4] By the grouping of WLS fibers to specific PMTs, modules are segmented in η and in radial depth. In the direction perpendicular to the beam axis, the three radial segments span 1.5, 4.1 and 1.8 $\lambda_{\rm int}$ in the barrel and 1.5, 2.6, 3.3 $\lambda_{\rm int}$ in the extended barrels. The resulting typical cell dimensions are $\Delta\eta\times\Delta\phi = 0.1\times0.1$ (0.1×0.2 in the last segment). The layout of cells is shown in Fig. 3. This segmentation defines a quasi-projective tower structure, where the deviations from perfect projectivity are small compared to the typical angular extent of hadronic jets. Altogether, TileCal comprises 4672 read-out cells, each equipped with two PMTs that receive light from opposite sides of every tile.

To reconstruct accurately the energy of the physics objects a precise and maintainable calibration of the calorimeter system is crucial. The design of the Tile Calorimeter includes a monitoring system for the scintillator and PMT response using a ^{137}Cs γ-source (Cs source), a laser system for the PMT and readout system response, and an electronic charge injection system for the readout electronics alone. These systems are described in more detail below and their performance during the test beam studies are reported. Several of them have been used regularly over many years.

To understand in detail the response of the final calorimeter modules about 11 % of the 192 modules were exposed to test beams of electrons, muons, and hadrons, ranging in momentum from 3 to 350 GeV/c in several test beam runs spanning four consecutive years. The main goals of this extensive testing program were:

(1) to set and measure the energy-to-charge conversion factors, using elec-

[4] Hamamatsu R7877 8-stage metal channel dynode PMTs.

tron beams. The settings will be reproduced on the untested modules by establishing similar Cs source responses on all modules,
(2) to explore the response uniformity of all modules with muon beams,
(3) to extend previous investigations on the response of the production modules to hadrons.

In addition, a number of general properties of the calorimeter were measured, mainly in view of its use within ATLAS.

The results of this extensive measurement program are described in this paper. In the remainder of this section, the main aspects of the module test beam setup and measurement program are reviewed, and the front-end readout electronics is briefly described. In the following sections, after discussing the TileCal energy reconstruction methods and the calorimeter calibration and monitoring systems, the performance of the calorimeter modules with electron, muon and hadron beams is described in detail. Summarizing the results of the test beam program, the concluding section dwells also on the implications of these results for the performance of TileCal in the ATLAS calorimeter system. Finally, measurements of certain system properties (response of the analog sum trigger, timing accuracy, recovery of electronics saturation) are briefly presented in three appendices.

1.1 Test Beam Setup

The calorimeter setup in the H8 beam of the CERN SPS North Area is shown in Fig. 4. Modules were placed on a scanning table capable of placing modules at any desired position and angle with respect to the incoming particles. The prototype Module 0 is the lowest in a stack of three modules. The middle layer is a production barrel module, and the top layer is either a pair of production extended barrel modules (as shown in the figure) or another production barrel module. Since part of the data are taken in projective geometry, module orientation is labeled according to η as in ATLAS, therefore for $\eta = 0$ the test beam is perpendicular to the front face of the middle module.

Calibration of each module consisted of taking data with beams in the following geometries:

- Beam incident at the center of the front face of each A-cell at $\theta_{\mathrm{TB}} = \pm 20^{\circ}$ from the normal ($\eta = 0$),
- Beam incident at the center of the front face of each A-cell, but at projective angles – e.g. at $\eta = 0.35$ in cell A4,
- Beam incident on the ends of the modules, into the center of each tile-row. This is referred to as 90° incidence.

Beam energies were usually between 20 and 180 GeV, with a few additional measurements below 20 GeV and at 350 GeV. The systematic uncertainty in the beam energy ranges from 2.5 % (10 GeV) to 0.5 % (350 GeV). For momenta between 3 and 9 GeV/c, a special tertiary beam was produced, by bringing the SPS secondary beam onto a target closer to the experimental setup. Typically, the H8 beam is a mixture of hadrons, muons and electrons. Particles were identified mainly by the calorimeter's response, however a pair of beam-line Cherenkov counters further assisted in particle identification.

Beam position was measured with three stations of x-y wire chambers, upstream of the module scanning table. Downstream of the module stack, a wall of muon counters helped tag muons and/or calorimeter punchthrough. The counters were routinely moved to be in the beamline for all orientations of the scanning table.

Triggering was a simple coincidence with three beam scintillation counters. The resulting spot size was typically 3x3 cm^2 or less. In addition to the beam trigger, several additional triggers (pedestal, charge-injection and laser-driven signals) were implemented and suitably flagged, for electronics calibration purposes.

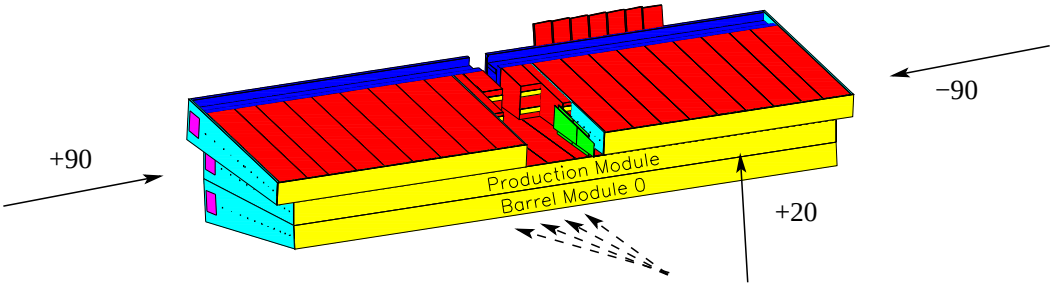

Fig. 4. TileCal modules as stacked on the scanning table at the H8 beam. The arrows indicate the beam directions used in the studies.

1.2 Signal read-out

The design of the TileCal front-end electronics is described in detail in Ref. [5]; only a few essential aspects are quoted here. The front-end electronics of each module is housed in a pair of extractable "drawers" (each pair being referred to as superdrawers), wherein the cell signals are digitized, the trigger tower analog sums are performed and the PMT currents are measured. The superdrawers also house the HV distribution to PMTs and monitoring and calibration circuitry.

The "3-in-1" cards, situated inside the iron magnetic shield of the PMT block, perform most analog functions of the front-end electronics. Bi-gain amplifiers produce shaped PMT differential signals with a gain ratio of 64. Both high-gain

and low-gain outputs are digitized within the drawers. This system measures energy depositions of up to 1.5 TeV in each readout cell; the least count corresponds to an energy of approximately 15 MeV. The shaped signals are sampled and digitized every 25 ns by 10-bit ADCs [6]. The sampled data are temporarily stored in a pipeline memory until a trigger level-1 accept signal is received. At the test beam, the level-1 accept is simply the beam scintillator coincidence, vetoed by the computer busy condition. The digitized samples are transfered from the drawer via an optical fiber link and recorded. In ATLAS the samples will be further processed in off-detector Read Out Driver (ROD) modules.

During normal data taking, 9 digitized signal samples were usually recorded. The ADC system normally forwarded either the high-gain or low-gain samples, depending on signal amplitude. In calibration mode, and in special runs, both high- and low-gain signals were read out.

The 3-in-1 cards also provide differential signals to the local Trigger Adder cards, which perform the analog sums of the signals within the trigger towers of every module. The sum has a 10-bit dynamic range. At the test beam, the outputs of the Adder cards were transmitted over twisted-pair cable to 8-bit flash ADCs, read out in a VME environment.

In addition, the 3-in-1 cards house programmable-gain operational amplifiers, acting as low-pass filters to smooth out the PMT currents. These quasi-DC signals are multiplexed within each superdrawer to a 12-bit ADC. The digitized signals are stored and read out over CANbus by the Detector Control System. These signals give the calorimeter response to Cs source scans, recorded during source calibration runs. In ATLAS running conditions, they will permit the monitoring of the response of each cell to minimum-bias interactions.

Throughout the test beam program all modules were equipped with final production electronics. The calibration and monitoring of the front-end electronics is described in Section 3.

2 Energy Reconstruction

Three different energy reconstruction methods have been developed and tested. The simplest and fastest of them, the "flat filter" method, has been used for the online event analysis. The more sophisticated "fit" and "optimal filtering" methods profit from knowledge of the pulse shape and provide better resolution, especially in the energy region where noise plays an important role [7,8]. These methods are described in the following sections, and some performance comparisons are given in Section 4.

2.1 Flat Filter Method

The flat filter (FF) method was the first to be developed. The N digitized samples S_i ($N = 9$ for physics events) are divided into two subsets. The first N_p samples constitute the "pedestal window"; the pedestal is the average sample value in this window. The subsequent $N_s = N - N_p$ samples constitute the "signal window". The signal is calculated as the largest sum of N_f successive samples within the signal window (see also Fig. 5):

$$s = \max_{j=N_p,N-N_f} \sum_{i=j+1}^{j+N_f} (S_i - ped) \tag{1}$$

More simply put, the FF method is just a sum over N_f samples; hence, it depends on the filter length N_f. For example, the sum with N_f equal 3 is 5 % smaller than the sum with N_f equal 5. The sum does not change significantly for $N_f \geq 5$, therefore the safe minimal value of N_f equal 5 is normally used.

For all readout channels, the timing is set to have the maximum signal in the 5th sample. At the test beam, the signal is not synchronized with the 40 MHz clock, hence its position can move by ± 1 sample. Therefore, $N_p = 1$ is normally used.

The FF method introduces a positive bias for signals that are almost compatible with noise because of the maximum in Eq. (1). After CIS calibration (see Section 3.2), channels without signal have an average amplitude of about 0.01 pC and an RMS of about 0.05 pC (respectively equivalent to ~ 10 MeV and ~ 50 MeV).

2.2 Fit Method

This method of signal reconstruction takes advantage of the knowledge of the pulse shape from the front-end electronics. This extra information is used to reduce the contribution of the electronics noise to the energy measurement, and allows a determination of the timing of the energy deposition. It also provides a measure of the quality of the reconstruction. With the fit method, when signals are in-time one can simply correct for signal saturation by using in the fit only the unsaturated signal samples.

For each channel, a fit is performed to the function $f(t) = Ag(t - \tau) + c$ to determine the three parameters: amplitude A, phase τ, and pedestal c, given a normalized pulse shape g. One minimizes the expression:

$$\chi^2 = \sum_{i=1}^{N} \left(\frac{S_i - [Ag(t_i) - A\tau g'(t_i) + c]}{\sigma_i} \right)^2 \qquad (2)$$

where the sum is over N digitized samples S_i having error σ_i, and each sample is measured at time t_i. The expression is a truncated expansion in the parameter τ. Figure 5 shows an example of the fitted pulse superimposed on the digitized samples of a given channel.

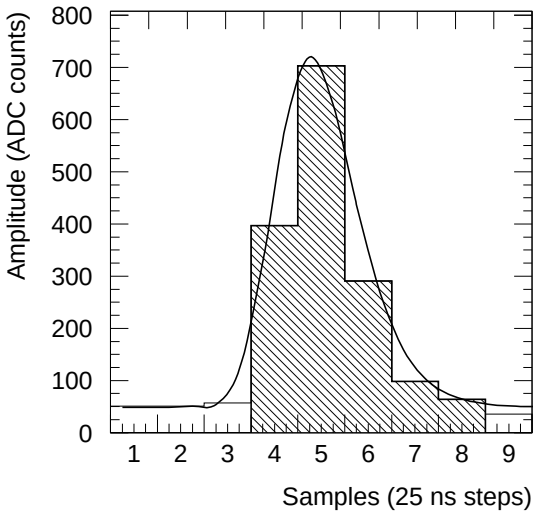

Fig. 5. Example of the 3-parameter fit method to the digitized samples of one channel. For comparison with the flat filter, the five samples giving the maximum sum are cross-hatched. In this case, nine samples were recorded.

Note that during ATLAS running the phase will be fixed, therefore in principle one could fit for only two parameters (amplitude and pedestal). A two-parameter fit is used in the case of small (pedestal-like) signals; here, to avoid the positive bias intrinsic to the FF method, the signal peak is set to the center of 5th sample.

The initial pulse shape is reconstructed by scanning over multiple events with varying phase.[5] The shape has been shown to be quite insensitive to the amount of energy deposited in the calorimeter and to the type of incident particle. Pulse shapes are derived separately for high- and low-gain channels, and separately for physics and calibration (CIS and laser) data. The resulting pulse shapes have a FWHM of 50 ns for physics events, compared to 45 ns for calibration triggers.

[5] The pulse shape was also derived from an electronic simulation of the shaper circuit, when introducing the standard PMT pulse shape on the input. The resulting pulse shape on the shaper output corresponds very well to that obtained directly from the testbeam data [9].

There is a scale difference among signals reconstructed with the fit and the flat filter methods; the pC/GeV conversion factor differs by 11 % in the two cases. In test beam data, the fit method gives a minimal offset, typically 0.2 fC ($\sim$ 0.2 MeV) per PMT, with all channels having an offset smaller than 1 fC. The Gaussian spread of the noise is 20 fC, which is an improvement of more than a factor of 2 over that of the flat filter. Furthermore, the fit method has been shown to give equivalent results whether 9 or 7 samples are recorded.

2.3 Optimal Filtering

The optimal filtering (OF) algorithm reconstructs the amplitude of the signal using a weighted sum of the digital samples. It also reconstructs the time and allows to estimate the quality of the reconstruction:

$$A = \sum_{i=1}^{N} a_i S_i \tag{3}$$

$$A\tau = \sum_{i=1}^{N} b_i S_i \tag{4}$$

$$QF = \sum_{i=1}^{N} \mathrm{abs}(S_i - A g_i) \tag{5}$$

N stands for the number of samples, A is the amplitude of the signal, τ represents the phase with respect to the expected sampling time (within the 5th sample). QF is the quality factor of the reconstruction. The parameters a_i, b_i are the OF weights for the amplitude and time reconstruction respectively. The values g_i are the amplitudes of the normalized shape function for the i-th sample and the S_i are the digital samples. The weights are calculated to reconstruct the proper magnitudes while minimizing the noise [10], using the Lagrange multiplier method.

It is envisaged to implement the OF algorithm in the firmware of the Read Out Drivers (RODs) – see Section 1. The simple arithmetical operations in the OF algorithm make it suitable for on-line data volume reduction in the ROD environment.

3 Calibration and monitoring systems

3.1 Calorimeter System Services

3.1.1 Low Voltage Power

During most of the test beam running the final low voltage system was still under development and the front-end electronics in each drawer was supplied using a package of commercial power supplies. These power supplies were adequate for the test beam but were not designed for the ATLAS environment. No remote monitoring was implemented with this system but the supplies were stable and performed well.

3.1.2 High Voltage Power

The Tilecal high voltage system [11] is based on remote HV bulk power supplies providing a single high voltage to each superdrawer. For each drawer there is a regulator system (HVopto card) that provides fine adjustment of the voltage for each PMT over a range of 350 V below the common input high voltage. This value is chosen to allow a broad range of adjustments around the nominal gain value of 10^5. One controller (HVmicro card) manages the two HVopto cards of the superdrawer. The monitoring and control system used in the test beam was based on VME. It had a LabView layer and PVSS-II, both running in a PC.

The high voltage of each PMT was monitored continuously during the four test beam periods in 2003. All voltages were recorded at 1 minute intervals and an alarm was triggered when a voltage deviated from its nominal value by more than allowed. The analysis of the high voltage data (excluding trips) shows that the fluctuations are small for almost all channels, with an RMS of $\sim$ 0.1 V, and a maximum deviation of 1 V. Since the PMT gain varies approximately as V^7, a 0.1 V drift in operating voltage corresponds to a 0.1 % gain variation at a typical voltage of 700 V.

3.1.3 Cooling

A special cooling system was developed for the electronics drawers and the front-end power supplies. A prototype version was tested during the calibration of Tilecal modules [12]. It supplied demineralized water to the modules at a flow rate of 60 l/h and a temperature of 18°C. The system was operated at sub-atmospheric pressure, which effectively supressed leaks. Studies were carried out in the test beam to evaluate the cooling unit and its influence

on the detector performance. The temperature stability and its effects on the calorimeter response are presented here, while other studies such as flow rate and an evaluation of the dissipated power of the superdrawers can be found in [12,13].

The response of the Tile Calorimeter depends on the temperature of its components, but by far the most sensitive element is the PMT. The goal is a PMT gain stability of 0.5 %. Previous lab measurements [14] have shown a dependence on temperature of $-0.2\,\%/^{\circ}\mathrm{C}$, leading to the requirement that the temperature of the PMT remain stable to within 2.5°C.

Temperature sensors monitor the input and output water temperatures as well as the temperatures of key components inside the superdrawers. Water temperatures were monitored during a five day period in the September 2001 calibration run[12]. A stability of 0.1°C (RMS) was observed which is fully sufficient for the requirements of the electronics. The temperatures inside the superdrawer were also monitored and again showed a very stable behavior. For example, the sensor at PMT 22 gave a mean value of 24.5°C with an RMS of 0.1°C.

A dedicated test was performed to evaluate the effect of temperature variation of the cooling water on the calorimeter response. The cooling water temperature was varied stepwise in the range of 16°C to 22°C, at a constant flow of 60 l/h. After a stabilization time of one to two hours the temperature inside the drawer was measured. The results indicate the following relation between cooling water temperature and PMT temperature:

$$\Delta T_{\mathrm{PMT}} = 0.74 \Delta T_{\mathrm{water}} \tag{6}$$

While the temperature of the cooling water was varied, a 180 GeV particle beam, principally pions and positrons, was directed to cell A14 to study the calorimeter response. This cell is read out by PMT 21 and PMT 22, and the latter is equipped with a temperature sensor.

The variation of the total measured charge versus the temperature of PMT 22 for pions and positrons is shown in Fig. 6. The two lines represent linear fits. The variation of the total signal and consequently the variation of the PMT gain is very similar for pions and positrons. This confirms that the gain variation is similar for all photomultipliers since the pion shower affects several cells and PMTs whereas the electromagnetic shower is mainly contained in a single cell read out by two PMTs. The final relation between signal variation and temperature of the PMT block is given by:

$$\frac{\Delta Q}{Q} = -0.2\,\%/^{\circ}\mathrm{C}_{\mathrm{PMT}}, \tag{7}$$

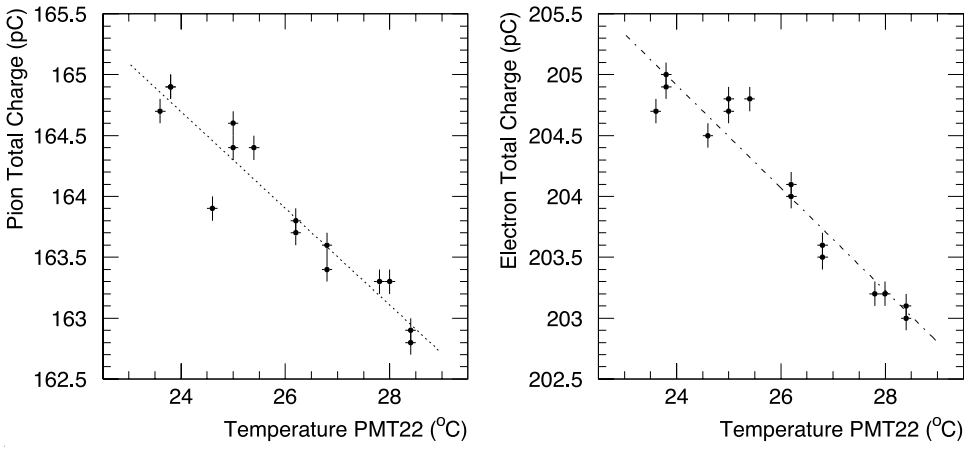

Fig. 6. Dependence of the total measured signal on the PMT block temperature for 180 GeV pions (left) and positrons (right). The slope of both lines is $-0.2\,\%/^{\circ}\mathrm{C}_{\mathrm{PMT}}$.

confirming the test bench measurements mentioned above [14].

Combined with the result of equation (6) the following relation for the gain variation of the PMTs is found:

$$\frac{\Delta G}{G} = -0.15\,\%/^{\circ}C_{\mathrm{water}} \tag{8}$$

Ensuring a PMT gain stability of 0.5 % requires a cooling water temperature stability of about 3.3°C, assuming that only cooling water temperature fluctuations contribute to changes in temperature of the PMT blocks.

3.2 Charge Injection System

As outlined above, the readout electronics for the fast pulses from each PMT contains two analog scales with a nominal gain ratio of 64. Each is digitized by a 10-bit ADC and together cover a range of charge to 800 pC. The charge injection system (CIS) is designed to calibrate the relative response of this system across all PMTs of the calorimeter and to track any variations with time. The goal is an accuracy of 1 %. The system is described in more detail in Ref. [5].

Each channel is equipped with calibration capacitors of 100 ± 1 pF and 5.2 ± 0.1 pF which can be charged from a high-precision voltage source and discharged into the input of the electronics. Both capacitors are charged from the same voltage source and hence can be intercalibrated. The resultant waveform at the ADC is similar to that produced by the PMT for a given charge but with a 10 % larger amplitude and 10 % smaller FWHM.

To determine the two gains in ADC counts/pC for each channel, dedicated CIS runs are taken which scan in discrete steps the full range of charges for both gains. To reconstruct the pulse amplitude using the ADC samples taken every 25 ns, a 3-parameter fit is performed, as described in Section 2. The fitted pulse shape includes a small bipolar component associated with the internal capacitance of the injection switch and the digital control signal. This is measured with zero voltage applied to the calibration capacitors. An example of the fitted pulse together with the digitized samples is shown in Fig. 7.

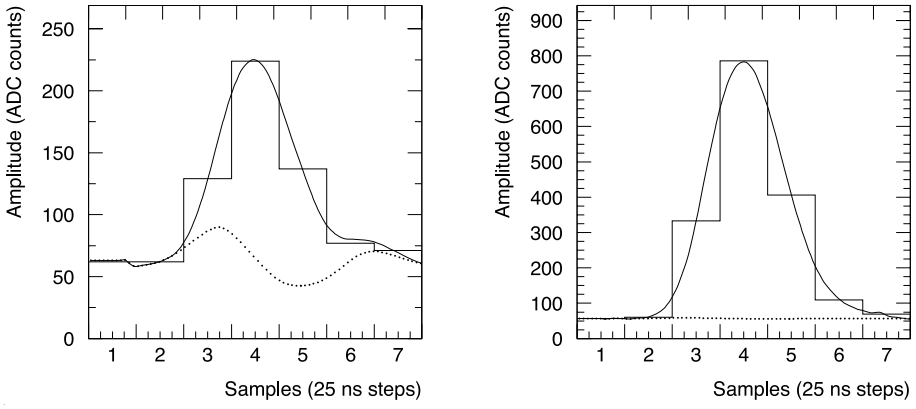

Fig. 7. Response to a CIS pulse of 2 pC (left) and 560 pC (right). The former is from the high-gain range and the latter the low-gain. The histogram shows the ADC samples and the solid line the overall fitted signal. The contribution from the capacitance of the switch is shown as the dotted curve. It is present in the CIS signals but not in physics signals.

The response of a channel as a function of injected charge is shown in Fig. 8 over most of the range of both gains. Both the total response and the residuals from linear fits are shown. The departure from linearity is typically no more than 2 counts over the active range of both scales.

The channel-to-channel variation of the measured gains has an RMS variation of 1.5 %, before applying any correction. This arises from the variations in the gains of the ADCs and of the PMT anode capacitances. During the 4-month-long test beam run of 2004, the corrected gains were stable at an RMS level of better than 0.2 %.

A careful study of the response of the readout system to the injected charge using the CIS system indicated a small but intrinsic nonlinearity in the response of all channels. This effect is negligible for very small and large charges but amounts to ~ 2 % at 100 pC. This correction was measured as a function of charge for a group of 269 channels and was applied in the analysis reported here. This same study concluded that the systematic uncertainty in the measured PMT charge arising from the electronic readout system is less that 0.7 % for pions and electrons of all energies reported here. This study is described

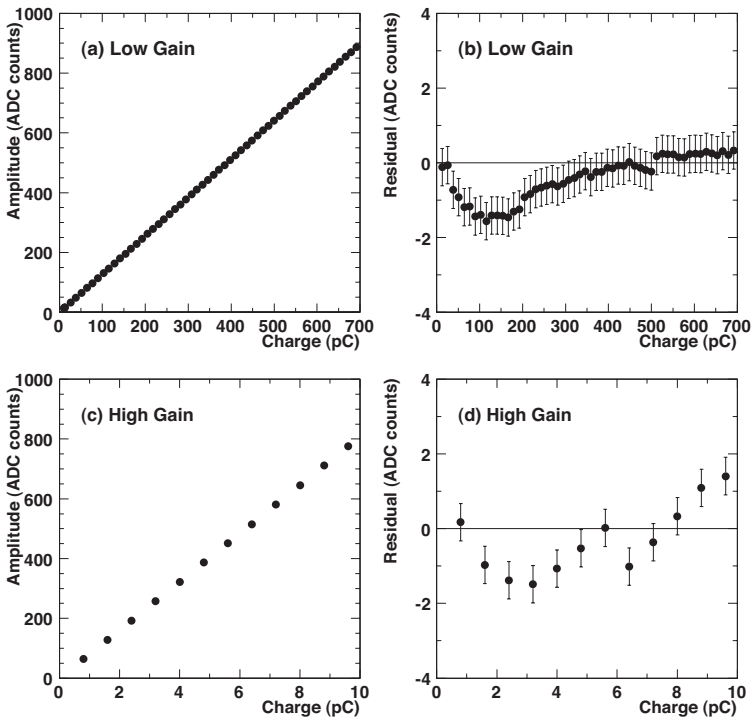

Fig. 8. Response of the high-gain and low-gain scales of a single channel to charge injection pulses. Plots (a) and (c) give the reconstructed amplitude as a function of charge, while plots (b) and (d) show the residuals. The error bars correspond to the expected differential nonlinearity of the ADCs. The fractional error associated with the residuals is small since full scale corresponds to 1023 counts.

in an internal ATLAS note [15].

3.3 Laser System

The laser system is designed to calibrate and monitor the response of the PMTs with an accuracy better than 0.5 %, both during ATLAS data collection and in special calibration runs. It is expected to be useful for debugging and diagnostic studies as well as to map individual PMT nonlinearities. Corrections could be applied for any significant nonlinearities.

A frequency-doubled Nd :YVO4 laser is used to produce light pulses with a wavelength of 532 nm and width of ∼10 ns, synchronized to the 40 MHz bunch crossing clock. The pulses are split close to the laser and a small fixed fraction is delivered to a set of photodiodes for monitoring the relative pulse-to-pulse intensity. The balance of the pulse is directed to individual PMTs through a dedicated set of clear fibers.

Monitoring the stability of the PMT gains is the system's most important

role. To demonstrate this ability a series of special calibration runs were taken during test beam operation. The charge delivered by the PMT for a given laser pulse was divided by the response of the photodiodes to provide a reference for the relative gain of each PMT. An average over at least 400 pulses was calculated in each run. Figure 9 shows the dispersion of the relative gains of 40 PMTs during 32 consecutive runs taken over a period of 3 days. The dispersion is the convolution of the drifts in gain, together with fluctuations of the measurements. It is found to be 0.5 %, showing that the PMTs are stable over the duration of the study and that the accuracy of the laser system matches the design goal.

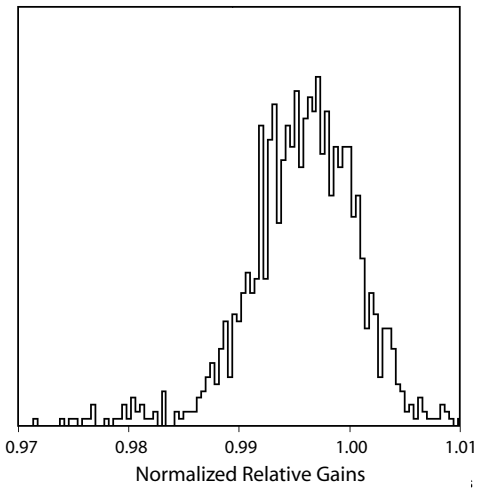

Fig. 9. Dispersion of PMT response as measured with the laser system for 40 PMTs over 32 runs.

The linearity of the PMTs can be studied by varying the intensity of the light to the PMTs. Although the intensity from the laser itself can only be varied by a factor of 10, an automated set of filters allows a dynamic range of over 1000. The global nonlinearity of the PMTs is found to be better than 0.3 % in the range 80 – 700 pC, 0.7 % between 5 and 80 pC, and 1.0 % in the region 0.7 to 5 pC. Special attention was paid to the area of transition between the high and the low-gain of the readout system but no unexpected effect was found.

The laser system can also be used to measure the absolute gain of each PMT. When this is combined with the measured response of the calorimeter in pC/GeV the photoelectron yield of the calorimeter can be obtained. The method takes advantage of the fact that the pulse-to-pulse intensity fluctuations of the laser are accurately tracked by the photodiode monitors; hence the remaining pulse-to-pulse variation of the PMT anode charge is simply related to photoelectron statistics and can be used to obtain the PMT gain. Specifically, it is shown in Ref. [16] that the product eG of the electron charge e and PMT gain G equals the mean value of $(q_p - q_t)^2/q_t$ over many pulses. This formula gives the mean square deviation of the measured anode charge

q_p from the expected charge q_t, which is calculated pulse-by-pulse from the measured photodiode signal. After taking into account the excess noise factor of the PMTs [17], the absolute gain of any PMT in the calorimeter is obtained. From the anode charges and the charge-to-energy calibration factors, the photoelectron yields are easily derived. In 2001, the light yield of all cells of an extended barrel module was measured, using both the laser system and muons incident at 90°. The results of these two methods of measuring the photoelectron yield are given in Section 4.1.

The laser system has proven to be useful for debugging and timing studies. It was also verified that it is powerful enough to deliver light simultaneously to the whole calorimeter.

3.4 Monitoring the minimum bias current

The hadronic calorimeter of ATLAS, like any other detector at the LHC, will face a background of inelastic proton–proton collisions at small momentum transfers. These processes lead to the so-called minimum bias (MB) events with a rate proportional to the LHC luminosity. The MB signals produce non-negligible occupancies in all Tile Calorimeter cells with rates which are moderately dependent on η and uniform in azimuthal angle ϕ. The rates vary substantially with depth in the calorimeter. The PMT anode currents associated with such events have been estimated by Monte Carlo calculations based on Pythia and GEANT3/G-CALOR. Results are given as a function of luminosity in Table 1. The luminosity values are given for early operation, nominal, and the ultimate scenario. The MB values are shown for the extreme cases of the A12 and D0 cells, and a typical case represented by the BC5 cell.

Fluctuations in the number of MB events per bunch crossing contribute directly to the noise term of the calorimeter energy resolution, specially for hadronic jets, where dozens of the calorimeter cells contribute to the signal. However, since the MB current, averaged over milliseconds, is almost constant [18], it can be used to monitor continuously the calorimeter response

Table 1
Response of three calorimeter cells to MB interactions. For each cell the following quantities are given for three luminosities: mean occupancy M and deposited energy E per bunch crossing; average PMT current I. Cell occupancy is defined as the probability that a signal greater than 1 MeV is observed in that cell.

Cell	$\mathcal{L} = 0.12 \times 10^{34}\text{cm}^{-2}\text{s}^{-1}$			$\mathcal{L} = 1.0 \times 10^{34}\text{cm}^{-2}\text{s}^{-1}$			$\mathcal{L} = 2.3 \times 10^{34}\text{cm}^{-2}\text{s}^{-1}$		
	M (%)	E (MeV)	I (nA)	M (%)	E (MeV)	I (nA)	M (%)	E (MeV)	I (nA)
A12	3.2	3.4	45	22	27	378	46	60	840
BC5	0.5	0.5	7	3.5	4.3	60	8.1	9.9	139
D0	0.0	0.0	0.2	0.1	0.1	1.4	0.3	0.3	4.2

during physics runs, without interfering with normal data acquisition. A variation in the ratio of the MB current to luminosity can be compared to information from the laser, charge injection, and movable radioactive source systems to understand the behavior of the calorimeter in time and to correct it. Alternatively, simultaneous analysis of a large number of calorimeter channels can provide a measure of the relative luminosity and the beam quality on a time scale of seconds.

For each channel of the Tile Calorimeter the PMT anode output is DC coupled to an operational amplifier with a fixed RC time constant of 10 ms, and a gain selectable remotely from six predefined values from 2.7 to 98 MΩ [5]. Because the range of MB current varies with the position of a cell in the calorimeter, as well as with the luminosity, to maintain an adequate resolution the gain of each channel is selected individually. The charge injection system described above is also used in conjunction with these circuits. It allows precise calibration and monitoring of the amplifier gains over the system's full dynamic range, from 12 pA to 1850 nA. Measurements of the six gains for each of the produced circuits give a dispersion of less than 1.4 % and nonlinearities of less than 0.3 %. The RC time constants were measured on a significant fraction of the channels and a dispersion of 1.1 % was found.

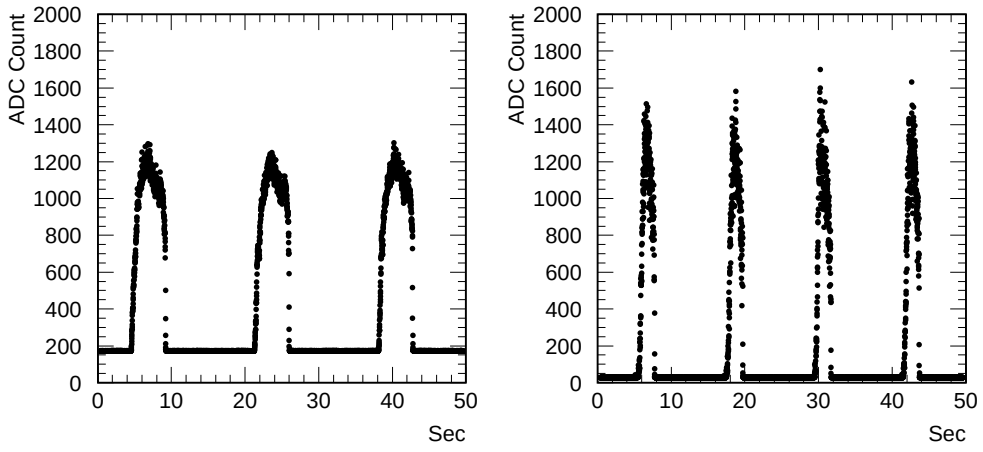

Fig. 10. SPS beam profile seen by the MB monitoring system for the two different spill structures mentioned in the text.

The operational amplifier outputs are multiplexed to a 12-bit ADC in each superdrawer, allowing measurements with a minimum resolution of 1 % for currents exceeding 1.2 nA. The ADCs are read out over CANbus and the data are stored into the ATLAS detector control system. In ATLAS, all ADC outputs in the Tile Calorimeter will be read out every 2 seconds.

The MB monitoring system was tested with hadron beams and with different particle rates, to emulate the conditions expected during ATLAS data taking and to check the adequacy of the system's dynamic range. The response

profiles shown in Fig. 10 were obtained with 180 GeV hadrons impinging at $\eta = 0.35$ on a barrel module. The signals are from a cell from the second radial depth segment of the calorimeter, and are plotted for two different spill times. The responses are consistent with expectations, based on the beam intensity, the average energy deposit in the second sampling, and the design of the MB system. The time structure of spills shown in Fig. 10 accurately reproduces the variations in time of the instantaneous beam rate independently observed during data acquisition, and constitutes further proof of the adequacy of the MB system for real-time monitoring of the TileCal cells.

3.5 Cesium Source System

The cesium calibration system is designed to measure the quality of the optical response of each calorimeter cell, to equalize the signal response from all cells, and to monitor it with time. The goal is to maintain the stability of the energy calibration at the level of 0.5 %. The system uses a ^{137}Cs γ-source ($E_\gamma = 0.662$ MeV, half-life $t_{1/2} = 30.2$ y) of 9 mCi and moves it through a hole in the scintillating tiles in a uniform, reproducible manner. The system has been described in detail in Refs. [19,20].

A metal capsule containing a 1-mm-long source is located in a water-filled tube running in a series of straight paths along the length of the calorimeter modules. It passes at normal incidence through holes in every scintillating tile and absorber plate of the calorimeter, as shown in Fig. 2. The capsule is driven by the water at a velocity of 25-30 cm/s. The current from each PMT is measured with the electronics described in Sec. 1.2 which samples at a rate of 90 Hz. Details of the electronics are described in Ref. [5]. Since the mean free path of the gammas from the source is comparable to the periodic 18 mm separation between tiles, the response of individual tiles can be clearly seen. The resolved peaks are typically measured with 6 points. Figure 11 shows the data from the scan of three adjacent calorimeter cells. The response of individual tiles is seen and a tile with poor optical coupling to the PMT is evident.

Two methods have been developed to characterize the response of a calorimeter cell. In the "integral method" the area under curves, such as those in Fig. 11 which corresponds to three readout cells, is evaluated and divided by the appropriate cell width. The integral is taken from a point ten 18-mm periods before the first maximum to a point ten periods after the last. For cells at a calorimeter boundary the unobserved tail is approximated from the signal at the opposite side of the cell, rescaled by the ratio of signal amplitudes at the two boundaries. The width of the cell, used to normalize the overall integral, is the distance between the first and last maximum in a cell plus one period.

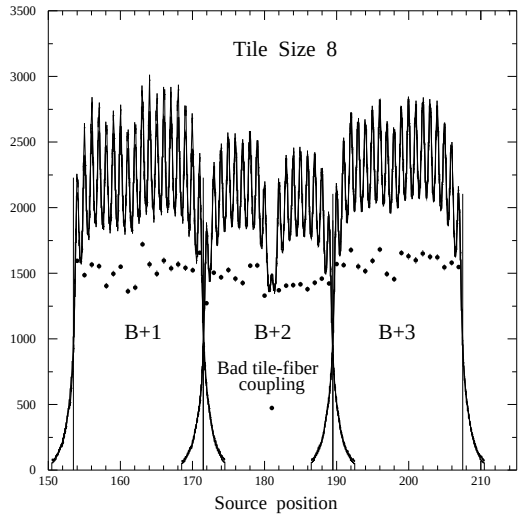

Fig. 11. PMT current as a function of source position measured in tile periods, for three adjacent cells.

The source also excites a significant amount of light in the row of scintillators adjacent to the one being calibrated and closest to the source path. In many cases the same PMT is coupled to both tile-rows so a correction must be made for the signal from the adjacent row. About 78 % of the energy is deposited in the row being calibrated while 22 % is from the adjacent row. The measured integral responses of row j is related the individual responses of the rows, I_j and I_{j+1}, by

$$I_j^{\text{meas}} N_j = 0.78 I_j N_j + 0.22 I_{j+1} N_{j+1}, \tag{9}$$

where N_j is the number of tiles in the cell of tile-row j. The calibration process gives a system of equations which can be solved for the individual responses I_j of each tile-row in each cell. The repeatability of the integral method is about 0.2 % for most calorimeter cells but slightly worse for the ITC cell C10 where there are only 5 tiles in a row and where both the left and right tails are anomalous because of local details in the steel structure of the calorimeter.

In the "amplitude method" a fit is performed to the response of individual tiles, characterizing the signal as the sum of a Gaussian and a symmetric exponential to describe the tails. This yields the signal amplitude for every tile in the calorimeter. The process starts with the tile-row at the edge of the calorimeter where there is no contribution from an adjacent row. In subsequent rows, the contribution from the adjacent row is already known and can be subtracted before the fit. The accuracy of a single tile response in this method is better than 2 % and the accuracy of the average amplitude of a cell is better than 0.3 %.

The integral method is faster than the amplitude method and is therefore used at the test beam for fast equalization of the cell responses by adjusting the

PMT gains. On the other hand, the amplitude method provides information for individual tiles and is used for special detailed scans when the quality of the module is checked. For the off-line analysis of the test beam data described here the amplitude method was used.

Equalization of the cell responses in the modules under test was performed at the beginning of every test beam period. During this process each PMT voltage is adjusted in an iterative process to reach a target value for the response from each cell. The first source scan is done with nominal HV settings corresponding to a gain of 10^5. The cell response is measured and new HV values are calculated with the formula:

$$\mathrm{HV_{new}} = \mathrm{HV_{old}}\left(\frac{\text{target response}}{\text{measured response}}\right)^{(1/\beta)} \tag{10}$$

The parameter β varies slightly from PMT to PMT, but the average value of $\beta = 7$ for all the PMTs gives convergence of the HV values to within 0.5 volts after three iterations. The target response was established in the year 2000 and adjusted in subsequent years for the decay of the source's activity. In 2002 the target value for cells in the third sampling layer of the barrel (D0, D1, D2, D3) as well as for cells C10 and D4 in the extended barrel was set to a 20 % higher value to improve the signal to noise for a level-1 muon trigger using those cells (see also Appendix A.1).

The short-term stability of the system has been established by taking an additional source run immediately after equalization of the cells. The variation in response for each cell has an RMS spread of about 0.2 %. If the system is switched off and the water drained and refilled, the ratio of new to old cell response has an RMS up to 0.5 %. This characterizes the level of precision for monitoring the long-term cell response and matches the design goal.

The ATLAS test beam run of 2004 spanned over four months of calendar time. This represents the longest undisturbed run of the production system to date. Figure 12 shows the variation of the response to the source over this period for 225 channels. No correction was applied to the high voltage to compensate for drifts in gain. The RMS spread in response after four months is 0.9 %.

The cesium source system allows an equalization of the calorimeter cells using the response measured near the outer edge of each tile-row segment where the source tubes pass through the scintillators. An important issue is whether this response is characteristic of the average response of the cell. To address the question, a laboratory study was done using a collimated ^{90}Sr source to map the variation in response of individual scintillators as a function of position [21]. This study showed that along a radial line through the center of the tiles, the amplitude of the total signal from the two PMTs increases by

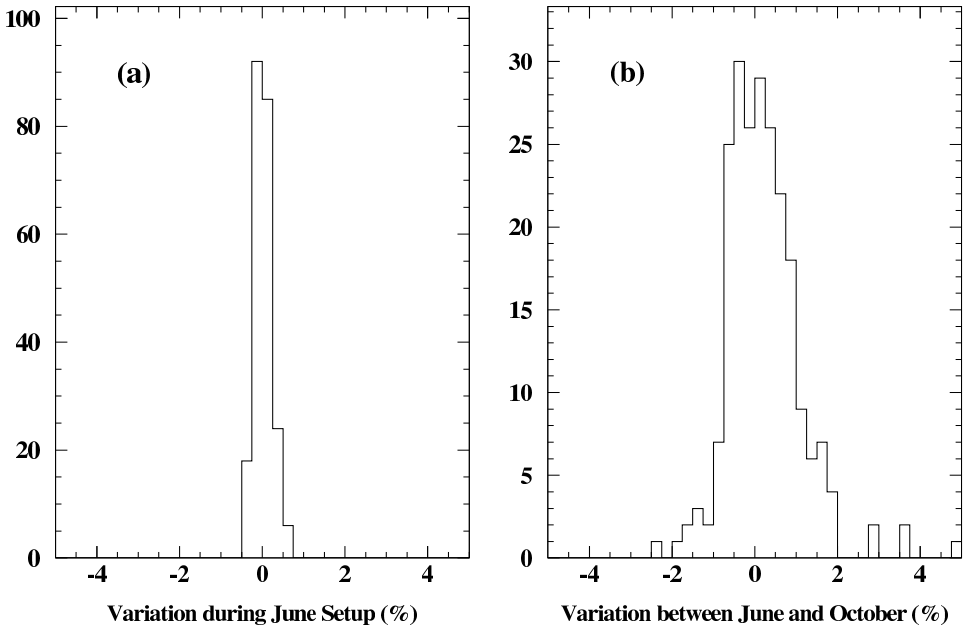

Fig. 12. Stability of the cesium calibration for 225 channels measured as part of the ATLAS test beam run of 2004. Plot (a) has an RMS of 0.2 % and demonstrates the short-term reproducibility of the system, while plot (b) shows an RMS variation of 0.9 % after four months of operation.

1 to 2 %/cm moving from the inner edge to the outer edge, independently of the tile size. As will be described below, the effect has also been confirmed in studies with beam particles, in particular with muons at 90°. Since the muon beam measurement uses the full calorimeter configuration and is very precise it has been used for the final correction factors (see Section 4.3.2).

4 Performance with particle beams

The principal goal of the Tile Calorimeter (TileCal) beam tests was to study the characteristics of the detector, exploiting the information that can be obtained with different particle types. Data were collected with beams of electrons, hadrons (pions, protons) and muons, at various incident energies and impact angles. Results on the light yield of the calorimeter are presented first, because photoelectron statistics results set a useful reference for the performance of a calorimeter. Next, after specifying the appropriate particle identification criteria, results are presented for each particle type. These include, where relevant, response and resolution versus energy and uniformity of response across the calorimeter.

Experimental results are compared to simulations performed with the GEANT4 [22] toolkit. Hadronic interactions are simulated with the Quark Gluon String Precompound (QGSP) and Bertini intranuclear cascade models [23]. Throughout this paper, use is made of version 8.3 of GEANT4, unless explicitly indicated otherwise.

The data analyzed here were taken after equalizing the cell responses by means of the Cs calibration system (see Section 3.5) and applying to the read-out electronics the calibration constants determined with the charge injection system (see Section 3.2).

4.1 Light Yield

The photoelectron yield of a calorimeter is one of the basic parameters characterizing its performance. It affects the signal-to-noise ratio, important for muon identification, as well as the energy resolution of the detector. In long-term operation, monitoring the photoelectron yield can be useful to track deterioration of optical components such as scintillator, WLS fibers and the PMT quantum efficiency. In the case of TileCal, its relatively high photoelectron yield is of great help in detecting isolated muons, although tests using prototype modules show that a photoelectron yield above 48 pe/GeV does not lead to improvement in the response to muons [3].

High energy muons incident at 90° traverse only one row of scintillating tiles, thereby providing a valuable tool to study in detail the photoelectron yield of TileCal modules. Muon beams of 180 GeV were used for this study. Based on Poisson statistics, the yield of any cell traversed by the muons can be calculated using the expression

$$N_{\mathrm{pe}}^{\mu} = \frac{\alpha \times C}{Q(u+d)} \times \frac{\mu}{\mathrm{e}} \times \frac{Q^2(u+d)}{\sigma^2(u-d)} \tag{11}$$

where N_{pe}^{μ} is the number of photoelectrons per GeV deposited by the muons in the calorimeter cell, $C = 1.25$ is the excess noise factor from the first dynode's gain fluctuations [17], $\alpha = 1.2$ pC/GeV is the TileCal energy calibration factor for electrons [6] at 90° (c.f. Section 4.2) and $\mathrm{e}/\mu = 0.91$ is the ratio of electron-to-muon response applying to this case [24]. The latter factor arises from the differences in energy loss mechanisms for electrons and muons. $Q(u + d) = Q(u) + Q(d)$ is the sum of the signals from the two PMTs that read out a TileCal cell, where u and d refer to the PMTs (Up and Down). The denominator $\sigma^2(u-d)$ stands for $\sigma^2\left[Q(u) - Q(d)\right] - \sigma_o^2\left[Q_o(u) - Q_o(d)\right]$, where

[6] This is the value of the electron response at 90° obtained with the flat filter method, which was used throughout the light yield analysis.

σ designates the RMS of the corresponding distributions and the σ_o originates from electronic noise and is calculated from the difference of the pedestal distributions.

In past analyses of TileCal data, $Q(u+d)$ was taken to be the most probable charge in the muon signal distribution [25–27]. However it can be easily seen that if a wide range of values around the peak of $Q(u+d)$ is used to calculate $\sigma(u-d)$, the latter will have contributions from a broad distribution of photoelectron numbers, and therefore will be overestimated. This will lead to an underestimate of the photoelectron yield. An alternative, more robust method was developed [28] and successfully applied to earlier data. It is referred to here as the "slice method".

The central region of the $Q(u+d)$ distribution is divided into several slices of equal ΔQ, as shown in Fig. 13 and $\sigma_i^2(u-d)$ and $Q_i(u+d)$ are extracted within each slice i. For each slice one may re-write Eq. (11) as

$$\sigma_i^2(u-d) = \frac{\alpha \times C}{Q_i(u+d)} \times \frac{\mu}{e} \times \frac{Q_i^2(u+d)}{N_{\rm pe}^{\mu}} + \sigma_o^2(u-d) \qquad (12)$$

which displays the linear relation between $\sigma_i^2(u-d)$ and $Q_i(u+d)$. The photoelectron yield $N_{\rm pe}^{\mu}$ is simply obtained from the slope of the linear fit. The slice method has two clear advantages over the earlier approach: the slices can be chosen so that the values of $\sigma_i^2(u-d)$ are independent of the slice width; and the constant $\sigma_o^2(u-d)$ may be obtained directly from the fit. In Fig. 13, a total of ten slices are defined, with similar event populations. It can be seen that the fitted line is rather insensitive to the chosen signal range.

The photoelectron yields shown in Table 2 are calculated with the slice method according to Eq. (12), using the central five slices. They are averaged over all cells of the four indicated groups of tile-rows and over a sample of six barrel modules used in the 2002 and 2003 test beam periods [29]. The scintillating tiles used in the construction of TileCal modules were manufactured by two companies, AKPO (polystyrene PSM-115) and BASF (BASF-165H), but with the same nominal composition. Table 2 clearly indicates that the BASF-tile light yield is about 25 % higher than that of AKPO tiles, in agreement with early laboratory measurements.

Note that these light yields are obtained from muons. The photoelectron yield for electrons is expected to be lower by a factor $e/\mu = 0.91$. For instance, for AKPO tiles the average light yield from electrons would be $N_{\rm pe}^{\rm e} = 72$ pe/GeV. It is worth verifying that this calculated light yield is as expected. Indeed, from the measured electron energy calibration factor of 1.2 pC/GeV and the nominal PMT gain of 10^5 one expects 75 pe/GeV for electrons, only 4 % higher than estimated from muon results.

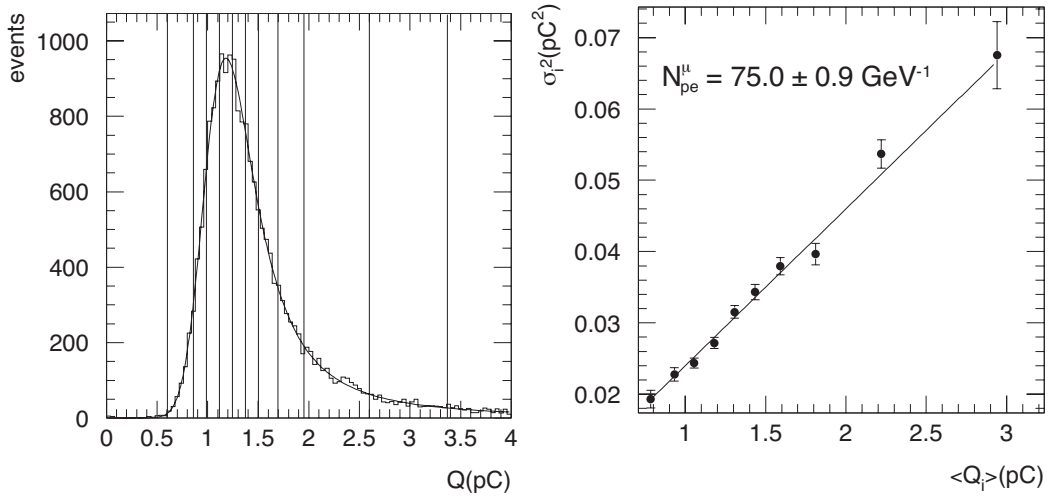

Fig. 13. Left: Calorimeter response to 180 GeV muons at 90°, with vertical lines showing the slices used in this analysis. The region from 0.86 to 1.5 pC is used for the primary analysis and the single region below and the four regions above are used as control regions. Right: fit using formula (12) to the values obtained from individual slices.

Table 2
The number of photoelectrons per GeV for 90° muons, in TileCal barrel modules. The average value for each cell type and the respective statistical errors are given separately for AKPO and BASF scintillators.

Tile-row	AKPO	BASF
$1-3$	78.0 ± 0.5	
$4-6$	79.0 ± 0.7	99.6 ± 1.0
$7-9$	80.1 ± 0.8	99.5 ± 0.9
$10-11$	79.2 ± 1.5	100.4 ± 1.1

The light yield has also been determined using laser data (see Section 3.3). Examining the light yield for one extended barrel module fully equipped with AKPO tiles, the laser analysis leads to an average light yield $N_{\rm pe}^{\rm laser} = 70.7 \pm 1.3$ pe/GeV, while the muon data give $N_{\rm pe}^{\mu} = 71.2 \pm 0.8$ pe/GeV. The results from the two independent analyses are in excellent agreement. The average PMT gain, measured with the laser system (see Section 3.3) is 1.16×10^5. This value is higher than the one quoted above for barrel PMTs, and corresponds to the fact that the observed light yields are significantly smaller than those given in Table 2. These differences reflect the fact that the best quality tiles were used for the barrel modules, while the extended barrel modules were instrumented with tiles having lower light yield [30]. Hence, higher PMT gains had to be chosen in order to obtain the same energy calibration factors for barrel and extended barrel modules.

4.2 Results with electrons

Whereas the scale of the response of the Tile Calorimeter to particles is first set and then maintained by means of the Cs source system, the calibration constant for electromagnetic showers – also referred to as the *electromagnetic (EM) scale* – must be determined by measuring signals of beam particles at known energies and calculating the average charge-to-energy conversion factor, in pC/GeV. For this purpose electron beams provide the obvious tool. Electrons are also used to verify the linearity of the response vs. energy and to test the detector uniformity and its energy resolution.

It will be shown below that the response to electrons varies significantly with the angle of impact, particularly at small angles θ_{TB}. For this reason, the primary calibration is established at a fixed angle of $\theta_{\mathrm{TB}} = 20^\circ$ ($\eta = 0.35$). Data with electron beams were collected in projective geometry at additional angles, as well as with the beam at normal incidence to the end plates of the modules ($\theta_{\mathrm{TB}} = \pm 90^\circ$).

4.2.1 Event selection

With all particle beams two sets of selection criteria were usually applied. For all particle types, single-particle events were first selected, using beam detectors upstream of the Tile Calorimeter (see Section 1.1).

Signals in the upstream scintillator counters were required to arise from single minimum-ionizing particles. This cut, especially useful for electrons, removed particles that initiated a shower upstream of the calorimeter, as well as two-particle events. Events where the beam chambers indicated tracks far from the beam axis and/or not parallel to it were rejected because they might have scattered upstream and therefore be off-energy.

The second set of selection criteria was specific to the type of particles being studied. This was necessary because the SPS H8 test beam is a mixture of electrons, hadrons and muons. For beam energies $E_{\mathrm{beam}} \geq 10$ GeV, muons were easily rejected by requiring the total measured energy to be $E_{\mathrm{tot}} > 5$ GeV. For electron/hadron separation,[7] two shower profile criteria were used. In addition, for energies of 20 GeV and below, an upstream Cherenkov counter was used to improve electron identification.

The shower profile parameters C_{long}, C_{tot} defined next exploit the difference of electromagnetic and hadronic showers profiles in the calorimeter. For ex-

[7] The electron-to-hadron ratio in electron beams ranges from 1:1.5 to 2:1 depending on the energy and fine tuning of the beam.

ample, if a particle enters the calorimeter at an angle of $\theta_{\rm TB} = 20°$, the first radial sampling corresponds to 14.3 radiation lengths and only 1.6 nuclear interaction lengths. The average energy fraction deposited in the first radial compartment by 100 GeV particles is therefore 89 % and 25 % for electromagnetic and hadronic showers respectively [31].

The variable $C_{\rm long}$ representing the longitudinal shower profile is defined as

$$C_{\rm long} = \sum_i \sum_{j=1}^{2} E_{ij}/E_{\rm beam} \tag{13}$$

where i runs over selected towers in $\eta \times \phi$ (typically in a 3×3 tower region centered around the beam), j represents the radial compartment number and E_{ij} stands for the energy in the cell (sum of the two PMT signals).

The variable $C_{\rm tot}$ represents an overall shower profile. It is defined as

$$C_{\rm tot} = \frac{1}{\sum\limits_c E_c^\alpha} \sqrt{\sum_c \frac{\left(E_c^\alpha - \sum_c E_c^\alpha / N_{\rm cell}\right)^2}{N_{\rm cell}}} \tag{14}$$

where E_c represents the energy in cell c and $N_{\rm cell}$ stands for the total number of cells considered. [8] The exponent α is tuned using a Monte Carlo simulation to achieve maximum electron/hadron separation; a value of 0.6 is used. All energies in Eqs. (13) and (14) are expressed in the same units, making $C_{\rm long}$ and $C_{\rm tot}$ dimensionless.

Distributions of $C_{\rm long}$ and $C_{\rm tot}$ are shown in Fig. 14 for a mixed electron-hadron beam of 180 GeV. The peaks on the right correspond to electrons, while the broad regions on the left correspond to hadrons.

Used together, these two quantities provide very effective electron/hadron separation, as demonstrated in Fig. 15. From these spectra one can estimate the hadron contamination in the electron sample after imposing cuts on $C_{\rm long}$ and $C_{\rm tot}$. The hadron admixture does not exceed 0.2 % in the 180 GeV beam. At 50 GeV and above, the separation cuts were tuned so that the hadron contamination never exceeded the value found at 180 GeV. Therefore, the admixture has negligible effects on the results shown in the next sections.

At energies $E_{\rm beam} \leq 20$ GeV the separation provided by these selection criteria is poorer [9] but the Cherenkov counter can be used to improve the purity of the electron sample. Typical scatter plots of the shower variables $C_{\rm long}$ and $C_{\rm tot}$ with respect to the Cherenkov signal are shown in Fig. 16 for a 20 GeV beam. Electrons are clearly separated from hadrons in both plots.

[8] As for $C_{\rm long}$, 3×3 towers in $\eta \times \phi$ are used for this cut, giving $N_{\rm cell} = 24$.
[9] The hadron admixture at 20 GeV is about 10 % after the shower profile cuts.

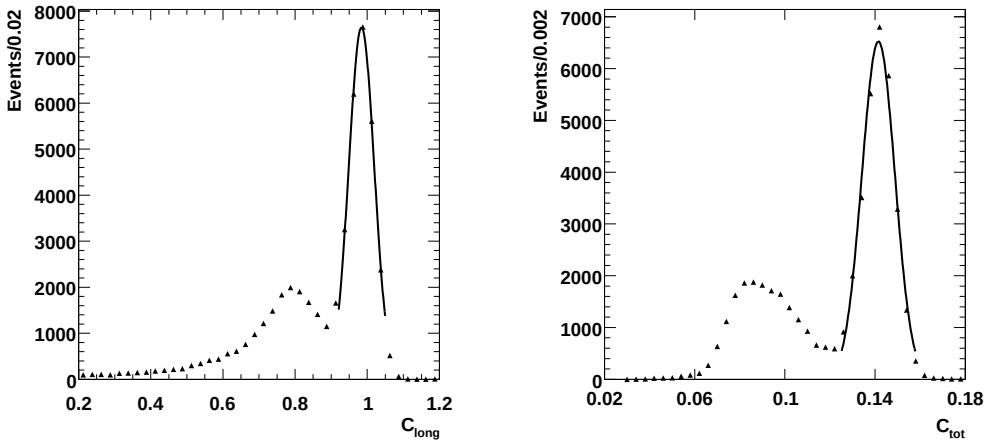

Fig. 14. Spectra of the longitudinal shower profile C_{long} (left) and of the overall profile C_{tot} (right) for 180 GeV beams. The Gaussian peaks on the right correspond to electrons, the broad regions on the left to hadrons.

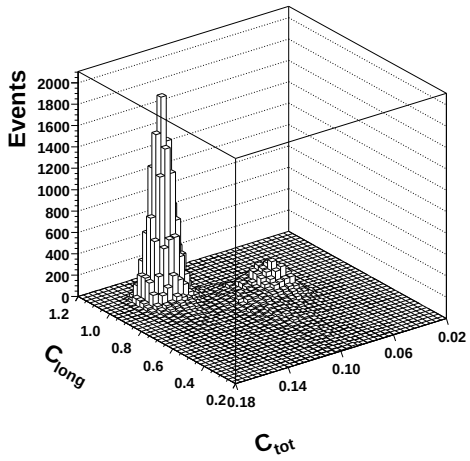

Fig. 15. The combination of the quantities C_{long} and C_{tot} used for electron/hadron separation at 180 GeV. The region on the left corresponds to electrons, the other to hadrons.

Instead of C_{long}, C_{tot}, some analyses used for electron/hadron separation a different shower shape variable, the *average density*, defined below in Section 4.4.1. The performance of the two methods is very similar.

4.2.2 Signal correction

Since the regularly spaced scintillating tiles lie in planes perpendicular to the LHC beams (see Section 1), the sampling fraction varies periodically with the impact point. Due to the compactness of electromagnetic showers, the electron response varies with the periodicity of the sampling fraction and thus depends

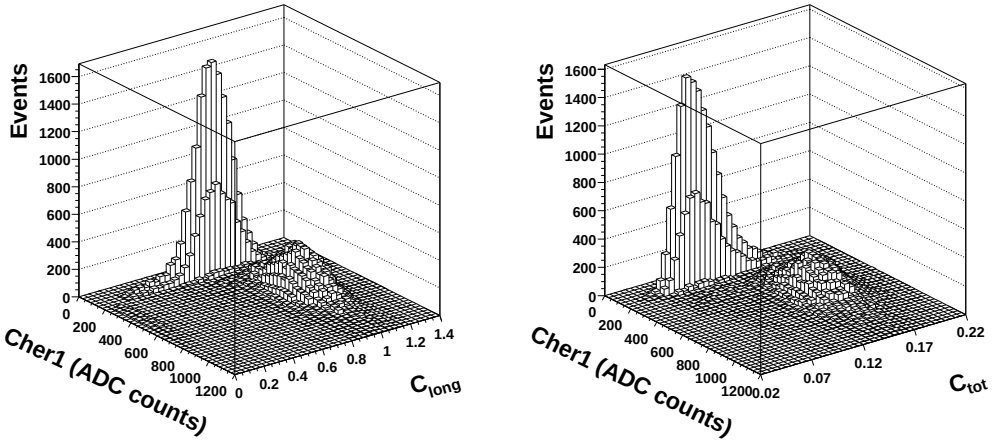

Fig. 16. Scatter plot of $C_{\rm long}$ (left) and $C_{\rm tot}$ (right) profiles vs. the Cherenkov signal for a 20 GeV beam. Electrons appear in the region with larger $C_{\rm long}$ ($C_{\rm tot}$) and high Cherenkov signal, while in the other region the Cherenkov signal is compatible with pedestal and is mostly populated by hadrons.

on the coordinate of the impact point along the front face of the calorimeter (Z). This is demonstrated in Fig. 17. The variation is reasonably well described by a simple periodic function

$$E_{\rm raw}(Z) = p_0 \left[1 + p_1 \sin\left(2\pi Z/p_2 + p_3\right)\right] \tag{15}$$

where p_0 corresponds to the mean energy and is used to evaluate the calibration constant. The parameter p_1 gives the relative amplitude of the oscillation. The variation decreases with increasing impact angle. [10] The parameter p_2 corresponds to the period thickness as seen by the beam [11] at the given impact angle and p_3 is a phase. The impact point coordinate Z is reconstructed using the beam chambers. With the above formula the observed oscillation effect is corrected for event by event and the Gaussian shape of the electron response is restored.

4.2.3 Comparison of signal reconstruction methods

The performance of the flat filter and fit method of signal reconstruction (see Section 2) were investigated with electrons. In the case of the flat filter, an additional correction was applied to individual readout channels to eliminate the spurious positive offset introduced by the method when the signal is small

[10] For example, at $\eta = 0.35$ (impact angle 20°) typically $p_1 \approx 0.05$, while at $\eta = 0.05$ ($\theta_{\rm TB} = 2.6°$) $p_1 \approx 0.2$.

[11] The value of p_2 scales with the angle of incidence as $P \times \cos(\theta_{\rm TB})$, as shown in Ref. [32].

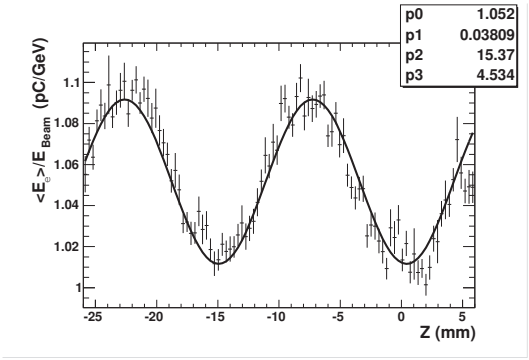

Fig. 17. The oscillation of the electron response due to the sampling fraction variation as measured at $\eta = 0.65$. The line indicates the fit of the equation (15), which is used to correct for the effect.

compared to the noise. [12]

The values of the calibration constants obtained with the two methods differ by about 11 %, as shown in Fig. 18. This is a consequence of the slightly different pulse widths of the CIS and physics signals (see Section 2 for more details). It has no direct impact on the calorimeter performance once this overall factor is taken into account.

As shown in the plot of Fig. 18, the channel-by-channel ratios of calibration constants obtained with the two methods agree at the percent level. These ratios exhibit an RMS variation of 1 %, which is significantly less than the cell-to-cell variation of the calibration constant (see Section 4.2.4).

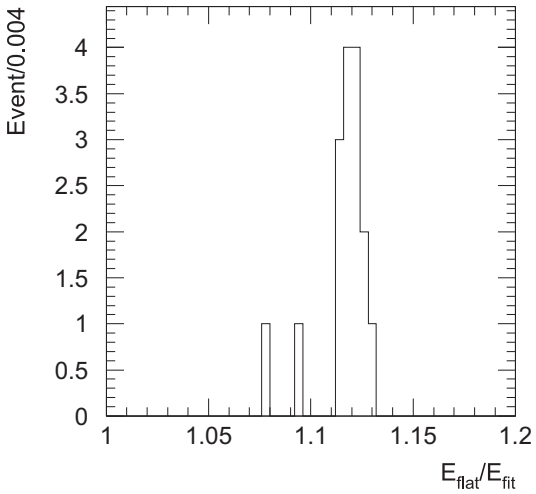

Fig. 18. Ratio of the calibration constants obtained with the flat filter and the fit methods from 180 GeV electrons at 20°.

The ratio of responses obtained with the two methods does not depend on the

[12] For a given readout channel, the mean offset relative to the pedestal is subtracted from signals less than $3\sigma_{ped}$ above the offset. Higher signals are not corrected.

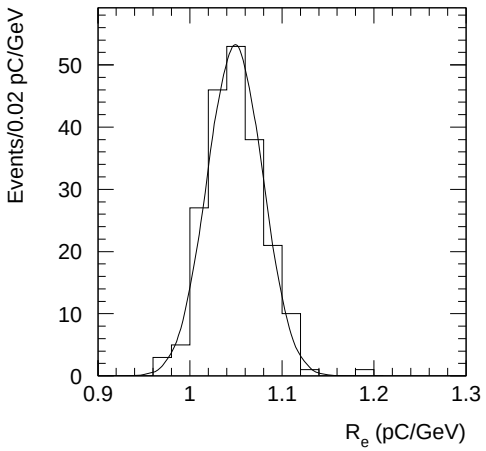

Fig. 19. The cell response of electrons at 20° (Mean = 1.050 ± 0.003 pC/GeV, RMS = 2.4 %), with one entry for each A-cell measured. The plot contains data taken at different electron beam energies.

beam energy, therefore their performance for electron linearity is the same. For the energy resolution, however, the fit method performs slightly better, as demonstrated in Section 4.2.7. Therefore all the results presented next were obtained with the fit method, unless explicitly stated otherwise.

4.2.4 Determination of the electromagnetic calibration constant

To obtain the EM calibration constant electron runs with energies from 20 to 180 GeV and with an angle to the front face of the calorimeter of $\theta_{\mathrm{TB}} = 20°$ were analyzed. The results only characterize the response of the A-cells, because in this energy range only a small fraction of the electron shower signal penetrates beyond the first radial compartment; other methods must be used to check the calibration at greater radial depths.

The analysis was performed on data from 3 barrel and 5 extended barrel modules; only runs where all channels were seen to be working were used. For each cell, the electron response was corrected for the variation with impact point described in Section 4.2.2. The distribution of the responses from about 200 cells is presented in Fig. 19. The mean value is 1.050 ± 0.003 pC/GeV (statistical error only) and is taken as the TileCal electromagnetic calibration constant. The cell responses vary with an RMS spread of 2.4 ± 0.1 %.

The dominant source of this spread is local variations in the tiles and in the light transmission efficiencies to the PMTs. These effects include the differences in the light yields of the tiles, nonuniformity of light collection within the tiles, variations in tile-to-fiber optical couplings, variations of the conversion efficiency and transmission in the readout fibers, and variation of the response across the PMT photocathode. Cesium source scans allow a precise

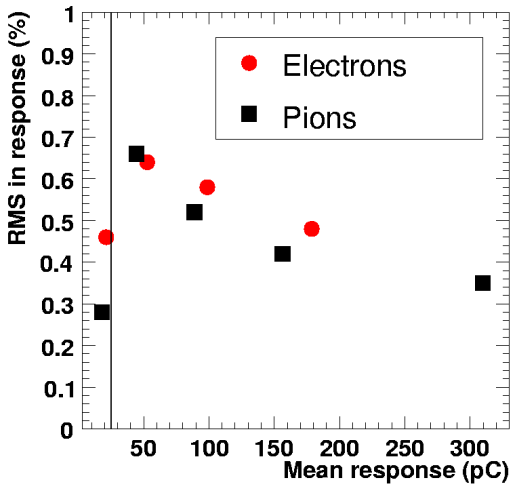

Fig. 20. The spread of the mean response to electrons and pions, caused by the systematics associated with CIS and ADC performance. The transition between high and low-gain readout channels is shown by a vertical line. At higher energies the spread for pions is smaller than for electrons, because pion showers are more diffuse and more channels are involved [15].

measurement of the individual tile response over an entire module. They show an RMS spread of 5 % (6 %) for a typical barrel (extended barrel) module [30].

The measured responses of the individual tiles to Cs in a production barrel module (JINR-55) were used to estimate the expected variation of the calibrated cells containing many tiles. The tile-to-tile variations were introduced into a Monte Carlo simulation of the response to electrons. Studies made for several energies and an angle of 20° showed a cell-to-cell variation among the A cells of 1.8 ± 0.1 %. This is to be compared to the RMS spread measured with an electron beam of 2.0 % (1.8 %) on the positive (negative) η sides of the same module. More details are given in [33].

Channel-to-channel differences of the readout electronics were found to play a smaller role in the variation of cell response. They include the systematic uncertainty of the CIS calibration as well as the differential nonlinearity of the fast ADCs. The total uncertainty is less than 0.7 % over the energy range from 20 to 180 GeV [15], as shown in Fig. 20. When measuring jets in ATLAS, this uncertainty is expected to be even smaller, because the signal will be collected from a larger number of channels.

Another small contribution is associated with the slow integrator electronics used in the Cs source system (Section 3.5). The related integrator calibration parameters were not used in the electron calibration constant analysis. Nevertheless, their RMS spread was measured to be 0.5 % [34,35], resulting in a very small effect on the EM calibration spread. In ATLAS, these constants will be used for the Cs source scans and may improve the EM scale precision

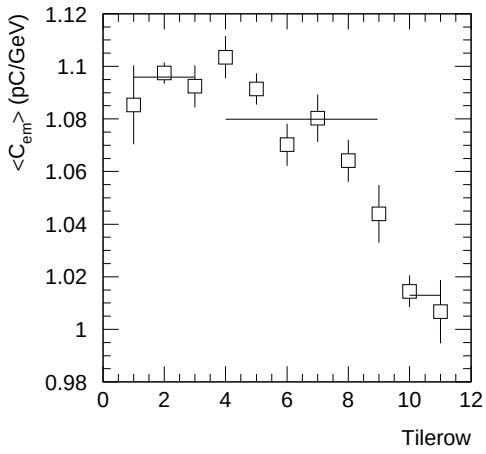

Fig. 21. The electron response relative to the beam energy as a function of tile-row number. Displayed is the response of 180 GeV electrons entering the barrel modules at $\theta_{\mathrm{TB}} = \pm 90°$, averaged over three different barrel modules. The error bars represent the error on the mean within the sub-cells of each tile-row. The horizontal lines indicate the average response in the individual radial compartments.

from 2.4 % to 2.3 %.

The value of the EM calibration constant established with 20° electrons in A-cells must be verified in the other radial compartments. This was done analyzing data with electrons incident at $\theta_{\mathrm{TB}} = \pm 90°$. The plot in Fig. 21 shows that there is a systematic variation of the response to electrons with tile-rows. The results in the figure were obtained averaging responses from three modules. This pattern is also observed with muons at $\theta_{\mathrm{TB}} = \pm 90°$, which unlike electrons allow a measurement of the response of cells through the entire volume of the calorimeter. Therefore the measurement of the EM calibration constant is taken up again, in the section on results with muons (4.3.2).

4.2.5 EM response versus pseudorapidity

The EM scale calibration constant presented in the previous Section is based on the analysis of electrons entering the calorimeter at 20°. As particles enter the calorimeter over a range of angles, the angular dependence of the EM calibration must be known too.

The EM shower response depends on the absorber thickness and (for equal sampling fraction) on the sampling frequency, i.e. the number of alternating active and passive layers per radiation length. This fact, sometimes called the transition effect (see e.g. Ref. [36,37]) is associated with low-energy (< 1 MeV) electrons, generated by the photoelectric effect in the absorber plates. These electrons may range out in the absorber plates and account for a significant

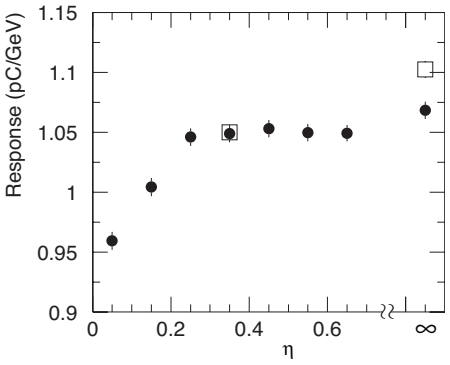

Fig. 22. The dependence of the EM calibration constants on the pseudorapidity. The results of the simulation for 20 GeV electrons is shown by full circles. Open squares represent two experimental points, for $\eta = 0.35$ ($\theta_{\mathrm{TB}} = 20°$) and $\eta = \infty$ ($\theta_{\mathrm{TB}} = 90°$). The simulated data are normalized to the experimental data at $\eta = 0.35$.

fraction of the energy of a shower. This effect reduces the signal from electrons at any given sampling frequency; but the higher this frequency, the more low-energy electrons reach the active material, thereby giving a signal.

The sampling frequency effectively changes with the angle of impact of the beam particles and the response to electrons changes accordingly. A simulation of this effect performed with GEANT4 is shown in Fig. 22. The experimental electron response at two angles of incidence is also shown in the same figure. [13] The simulation is normalized to the experimental result at $\eta = 0.35$ ($\theta_{\mathrm{TB}} = 20°$).

The simulation shows a drop in response for $\eta < 0.25$ which can be qualitatively understood as the effect of the periodic tile/iron structure of the calorimeter on tightly collimated EM showers. Overall, the Monte Carlo (MC) predicts a variation of the EM calibration constant of about 10 % over the full range of angles of incidence, of which only about 2 % takes place between $\theta_{\mathrm{TB}} = 20°$ and $\theta_{\mathrm{TB}} = 90°$. In contrast, experimental data show a difference of 6% over the latter range. This is semi-quantitatively explained by the fact that the response at the center of tiles, hit by beams at $\theta_{\mathrm{TB}} = 90°$, is 3.5 % higher than the response averaged over its surface. These tile response measurements are described further in [33] and references therein. For data taken in projective geometry with $\theta_{\mathrm{TB}} < 90°$ the secondary particle paths are distributed over a larger area of the tile surfaces, so a smaller signal with respect to that at $\theta_{\mathrm{TB}} = 90°$ is expected. The surface nonuniformity of tile response is not simulated in the Monte Carlo study described here.

[13] As discussed previously, the spread of the measured electron responses, due to optical component nonuniformities (Section 4.2.4), makes it hard to detect a small EM scale angular dependence. Therefore only experimental points at 20° and 90° are shown here, since they represent averages over a large number of runs taken on many different calorimeter cells.

In the experimental situation of ATLAS, the angular variation of the response to electrons is not an issue, because the liquid argon electromagnetic calorimeter upstream of TileCal will almost entirely absorb the energy of EM showers, while TileCal will will detect mainly the energy of hadronic showers. The angular response of hadronic showers is addressed in Section 4.4.3.

4.2.6 Linearity

In order to define a unique EM calibration constant the response of the calorimeter to EM showers must be linear to a good approximation.

The linearity of the Tile Calorimeter's EM response can be characterized by the ratio of the signal (in pC) to the beam energy (in GeV) over a range of electron beam energies. This is shown in the left panel of Fig. 23 for three different barrel modules and for energies in the range of 10 to 180 GeV; the angle of incidence of the electron beam is $\theta_{\mathrm{TB}} = 20^{\circ}$. In obtaining these ratios care was taken to use the precise value of the electron beam energy seen by the modules; this was calculated using the actual settings of the beam line's bending magnets and collimators, and taking into account the upstream bremsstrahlung losses at each beam energy. The differences with respect to the nominal beam energy were up to 0.5 %. No correction was made to the data for the mean energy loss in the TileCal iron front plate, which is 1 cm thick ($0.6X_0$). However, this material is included in the Monte Carlo description of the calorimeter and its influence on the energy dependence of the response can be seen in the solid line in the right panel of Fig. 23.

The considerable spread of calibration constants shown in Fig. 23 can be mostly attributed to the local variations of optical response that generate the spread of cell calibration constants discussed previously. Similarly to what was shown in Section 4.2.4, this was demonstrated with a specific simulation in which all the individual tile responses of the same previously mentioned module (JINR-55) were introduced into the Monte Carlo code. The results of this simulation are displayed in the right panel of Fig. 23, where the responses for five beam impact points spaced by 1 period (18 mm) along the Z-axis are given. In the plot one can also see the linearity of an ideal module, in which all tiles have the same response. From the simulation one can draw the following conclusions:

- Even in an ideal module the EM response displays a small nonlinearity of about 0.5 % from 10 GeV to 180 GeV. This is mainly due to the iron front plate.
- The tile-to-tile variations make it hard to detect intrinsic deviations from the linearity of the response to electrons unless one can reproducibly aim the electron beam into the same calorimeter points with an error of less than 1

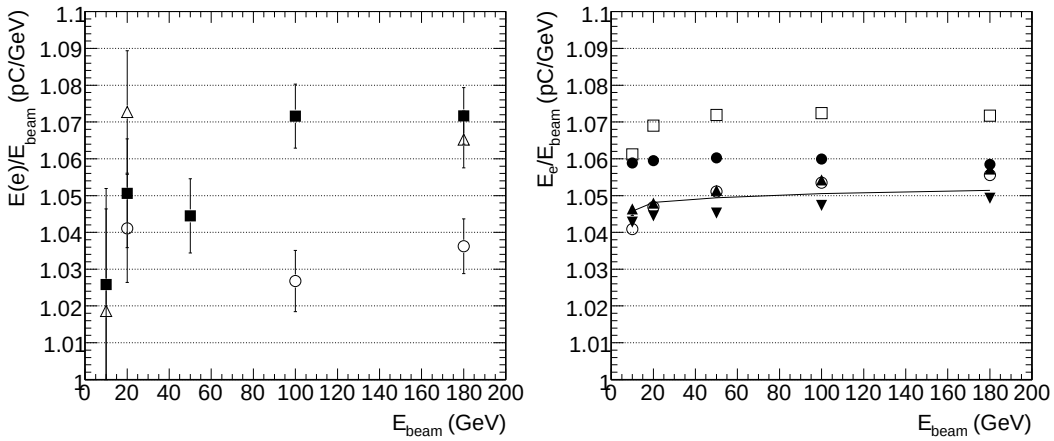

Fig. 23. The linearity of the response to electrons at $\eta = -0.35$. Left panel: Signal/beam energy in three different barrel modules. The error bars include the uncertainty due to the calibration (see Section 4.2.4) as well as the systematic uncertainty in the beam energy. Right panel: Simulation of the response vs. energy introducing the response measured for all tiles in a production module. Different symbols correspond to five different impact points, spaced by 1 period. The continuous line shows the calorimeter response in the absence of local differences of tile response.

cm. If the beam impact point were the same at all energies the nonlinearity would be within 2 % whereas if the impact point is different at different energies the nonlinearity increases to about 3 %.

In the TileCal test beam the position in Z of the table carrying the modules was not reproducible to better than 1–2 cm and the data taking mode was such that the table would typically be moved several times between electron runs at different energies. Therefore it is not surprising to encounter responses as in the left panel of Fig. 23.

In summary, the ± 3 % fluctuations with respect to linear behavior observed in electron data can be mostly explained on the basis of tile-to-tile differences.

4.2.7 Energy resolution

High-energy electrons will not be detected by TileCal as installed in ATLAS, but resolution studies are useful nonetheless to understand the characteristics of the calorimeter. In particular, the stochastic term in the parametrization of the resolution as a function of energy provides a lower limit to the value of the same term when measuring the resolution for hadrons, and the constant term must be compatible with the measured variation of cell response.

First a comparison is made among the resolutions obtained with the flat filter and fit methods. Results with 20° beams are shown in Fig. 24. The resolution

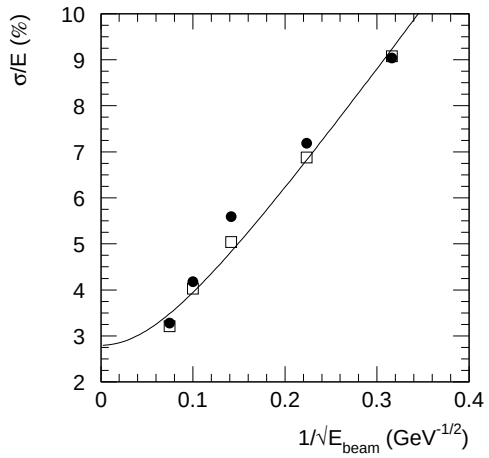

Fig. 24. The energy resolution for electrons at 20°. Full circles denote the flat filter results, while open squares correspond to the fit method. The fit with formula (16) applies to the fit method results.

with the fit method is found to be similar to or better than that of the flat filter, the biggest difference occurring for the medium energy range. This is as expected because these energies correspond to the transition between high and low-gain electronic channels. Since the resolution with the flat filter is worse for very small electronics signals, it deteriorates significantly for signals just above the threshold of the low-gain electronics. The energy resolution scales with the energy approximately as

$$\frac{\sigma}{E} = \frac{a}{\sqrt{E}} \oplus b \tag{16}$$

where the symbol $\oplus$ indicates the sum in quadrature. The fit displayed in Fig. 24 applies to the resolution obtained with the fit method and gives $a = 28\,\%$ GeV$^{-1/2}$, $b = 2.8\,\%$. The beam momentum spread has practically no influence on the above results, since the relative RMS is below $0.8\,\%$ for all energies. The value of the constant term is comparable with that of the local variation of response described in Section 4.2.4.

4.3 Results with muons

The high-energy muons available at the H8 beam line traverse the entire TileCal modules for any angle of incidence, thereby allowing a study of the production module response in great detail through their entire volume. The results of these studies are the main subject of this section.

The most important application of muon data is the measurement of the response of cells as a function of radial depth, which allows setting the EM scale obtained with electron beams in the first radial compartment in the

other two compartments. In addition, the response to muons at 90° can be measured for each segment of a tile-row within a cell (tile-row segments can be seen in Fig. 3). The Cs source calibration information is also available with the same high granularity and can be used to sharpen the understanding of the response of the calorimeter.

Other issues analyzed in this section are the response to muons in projective geometry and to very low energy muons at 90°.

4.3.1 Event selection and signal correction

The data analyzed here were taken with 180 GeV muon beams, either in projective geometry or at 90°. In the latter case, the entire radial span of several modules was probed with a series of muon runs with the beam centered, in turn, on each of the 11 tile-rows of a module. These scans produced responses from about 2000 tile-row segments of 488 calorimeter cells, representing about 10 % of the detection volume of the entire ATLAS Tile Calorimeter system.

Triggers were selected to be loosely consistent with muon signals by requiring between 1.2 pC and 50 pC in both the first and second halves of the central barrel modules or 1.2 pC to 46 pC for the shorter extended barrel modules. In addition, tracks measured in the beam chambers were required to be nearly collinear to the beam line. For the projective data at fixed η, the muon response was corrected according to the position of the particle impact point. As discussed in the section on electron beams, this correction accounts for the variation in the calorimeter sampling fraction [24] and significantly reduces the spread of the muon signal, particularly for incidence at small $|\eta|$.

The TileCal response to high-energy muons follows a Landau-type distribution with characteristically long tails at high energies caused by radiative processes and energetic δ-rays. The peak values of the muon signals under study vary by more than a factor of two in projective geometry and by more than an order of magnitude for 90° incidence, because of the different sizes of cells in modules. The interplay of the high-energy tails and of the variation in cell length results in very different values for the muon signal depending on how it is defined. The most obvious definition, namely the most-probable (peak) value of the signal divided by the muon path length, displays a significant residual dependence on the path length that makes it unsuitable for studies of the calorimeter response uniformity. Instead, the mean value of the measured muon energy loss spectrum truncated at 97.5 % of the total number of entries was adopted. This definition of the calorimeter response to muons was found to scale with the muon path length, with minimal residual corrections.

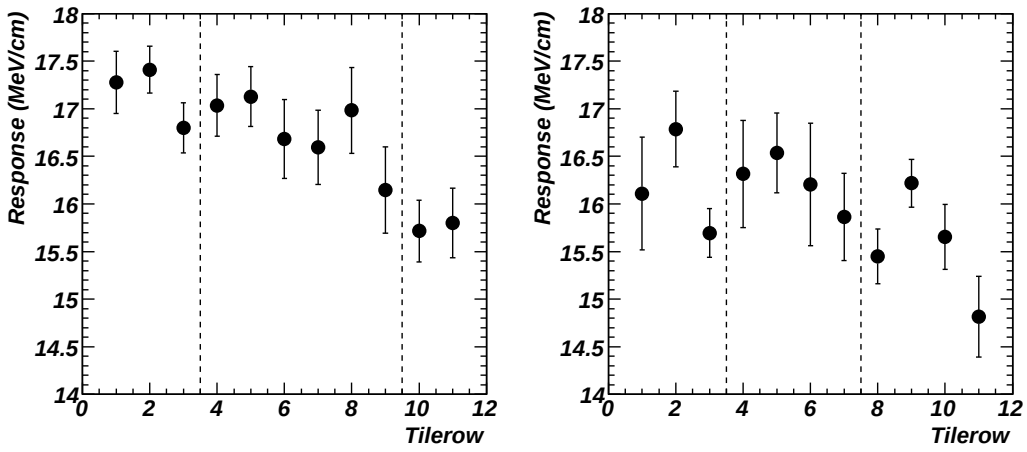

Fig. 25. The signal per unit path length produced by 90° muons incident on individual tile-rows, averaged over all analyzed modules. Data are shown for barrel modules (left panel) and for extended barrel modules (right panel). The error bars represent the tile-row RMS spreads over modules and the dashed lines indicate the separation of individual radial compartments of the calorimeter.

4.3.2 Measurement of the EM calibration constant with 90° *muons*

A precision analysis of the response to 90° muons vs. tile-row number was carried out in order to extend the measurement of the electromagnetic calibration constant to the entire radial depth of the TileCal modules.

Within each tile-row, signals were summed over the whole length of the barrel or extended barrel modules.[14] This approach avoids the small systematic effects due to the residual signal dependence on the muon path length and the decrease of radiative muon energy losses along the muon track.[15] The response to muons incident on each tile-row is shown in Fig. 25, where the muon signals are averaged over all modules exposed to the muon beams. The signals are expressed in units of energy per unit muon path length, obtained applying the EM scale calibration of 1.05 pC/GeV and the ratio of electron-to-muon response (e/μ) for 180 GeV muons mentioned in Section 4.1.

The muon response clearly depends on the tile-row number. Note that the same pattern is also observed with electrons incident at 90°, as shown earlier in Fig. 21. In order to obtain a uniform calibration of the response on the EM scale different multiplicative factors must be applied to the signals from

[14] The length of the muon path in all 11 tile-rows is the same in the barrel, and also in the the extended barrel modules when the special cells C10, D4 are excluded from the analysis.
[15] The latter decrease is about 2.5 % along the 6 m length of the 90° muon path in Barrel modules.

Compartment	Barrel	Extended barrel
1	1.000	1.000
2	1.025 ± 0.002	1.009 ± 0.005
3	1.088 ± 0.005	1.055 ± 0.003

Table 3
The correction factors that cancel the radial dependence of the response to 90° muons, averaged over several analyzed modules. The statistical errors are also indicated.

the three radial compartments.[16] The factor for the first radial compartment (A-cells) is set to one, in order to preserve the EM scale as determined with 20° electrons. The weights in the second and third radial compartments are evaluated as the inverse ratio of the mean muon responses in the respective tile-rows to the mean responses of the three A-cell tile-rows. The factors are given in Table 3. Although the observed muon signal patterns are the same in the barrel and extended barrel modules, the factors differ due to their different radial segmentation (see also Fig. 3).

In Fig. 25 one can observe a difference between the size of muon signals in barrel and extended barrel modules. This is due to its residual dependence on the muon path length within a cell. This feature is fully reproduced in MC simulations.

It is worth noting that the observed variation of the muon signal with tile-rows is well understood. The initial equalization of the PMT signals from different cells is based on the response of every tile-row to the Cs source signal and on the assumption that it characterizes the response of the scintillators to EM showers. However as mentioned in Section 3.5 the response of tiles is not uniform across their surface – instead, near their outer edges (where the Cs signals are produced) the response is greater than at the center, by about 1 %/cm radial distance from the center (where 90° muons and electrons were directed) [21]. Hence the difference between the Cs and 90° muon signals is larger for the larger tiles situated at greater radii, shown in Fig. 3. On the other hand, as already mentioned in Section 4.2.5, the response of tiles at their center is 1.035 times higher than their response averaged over the whole surface, and this ratio is the same for all tiles [33]. Therefore the response to 90° muons provides an unbiased measurement of the response of cells, and must be used to correct the cell intercalibration based on the Cs source signal.

It is also worth pointing out that the differences in response over the tile surface, measured in the lab, are in good quantitative agreement with the

[16] Individual tile-row corrections cannot be applied for beams entering at projective pseudorapidities, because the signals from all the tile-row segments belonging to a given cell are added into the same PMT.

correction factors given in Table 3.

In addition, the correction factors established here are consistent with observations on the response of muons measured in projective geometry, as shown later in this section.

It should also be stressed that properly setting the EM conversion factor for all cells of the calorimeter is crucial for obtaining the proper response to hadrons.

4.3.3 Uniformity of response within modules and across modules

The muon response from the 11 different tile-rows varies not only due to the difference between the response to particles and to the Cs source signal, but also because of variations in individual tile/fiber light-yields and the differing layouts of the WLS fibers as already described in Section 4.2.4.

Part of this variation arises from response differences among the tile-row segments forming a calorimeter cell. The Cs source calibration procedure (see Section 3.5) equalizes the responses of overall cells but signals from tile-row segments within a cell may differ by a few percent. Since muons in the 90° configuration only excite individual tile-row segments, their Cs source response can be used to partly remove this variation.

In doing this analysis one must take into account further systematics that affect the muon response. The most important effect is that the average signal from the first cell traversed by muons is lower than that from the next cells. This is due to the fact that the EM showers associated to large radiative losses or to very energetic δ-rays, which can take place in any cell, will partially be deposited in subsequent cells. Therefore the muon signal in the first cell is up to 10 % lower than in subsequent cells, depending on the cell size. To avoid this bias the cells first traversed by muons are excluded from the tile-row segment uniformity analysis. Smaller systematic effects are associated with the residual truncated mean dependence on the cell size and with the variation of radiative energy deposit along the muon tracks. These effects are reproduced by MC simulations and were corrected based on simulation results.

The results of this analysis for all eight barrel modules exposed to muons are shown in Fig. 26. In the left panel are plotted the mean responses of tile-row segments within each tile-row to muons, corrected for the systematic effects just described and normalized to the average response within the first radial compartment. The error bars represent the RMS spread of responses within each tile-row; they are 3 % to 5 %. The overall variation of the mean responses over the 11 tile-rows is about 10 %, the same result seen in the preceding section. In the right panel, the response of each tile-row segment has been corrected by the corresponding normalized Cs source result. The RMS spread

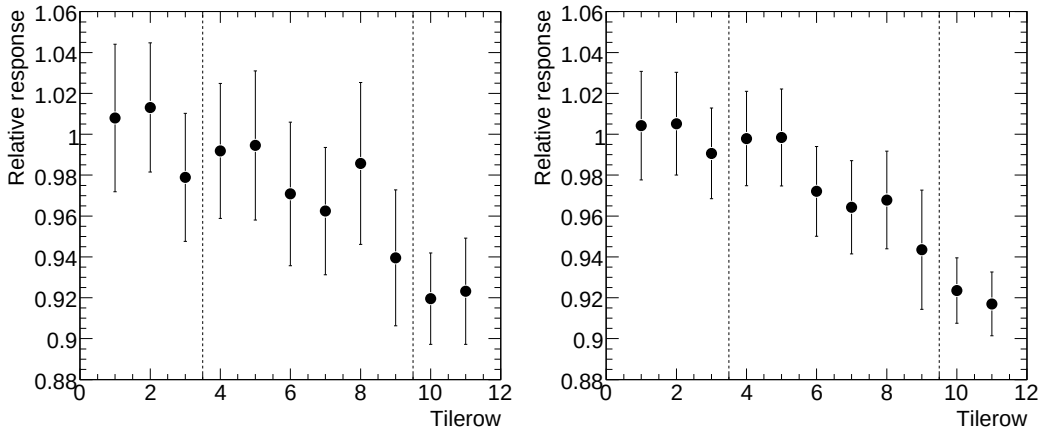

Fig. 26. Left panel: mean responses of tile-row segments to muons at 90° from eight barrel modules. The responses are normalized to their means in the first radial compartment. Right panel: the same, corrected by the Cs source results in each tile-row segment. The error bars represent the RMS spread of the results used to obtain each point, the dashed lines indicate the separation of individual radial compartments of the calorimeter.

within tile-rows is reduced to about 2 %, and the overall variation of the 11 means is now about 8 %.

The variation between tile-rows observed after correcting for the Cs source information is due to two separate components:

- The radial dependence of the signal, just discussed.
- Well-understood effects of light transmission within tiles and/or WLS fiber layout.

The response variation between tile-rows is also compared with electrons and muons. Figure 27 shows the average response for both particle species, corrected by the Cs source tile-row segment signals in the same way as in Fig. 26. The data are normalized to the mean response in the first radial compartment. The results clearly indicate a consistent behavior as a function of the tile-row number.

Finally, a summary of the responses to muons observed over seven test beam periods from 2001 to 2003 is given in Fig. 28. The results are from all tested modules (eight from the barrel and thirteen from the extended barrel). Each barrel module (except for one) is represented by two points, one for each superdrawer. The averages of the muon responses for all tile-row segments of each module are shown. Their overall stability is guaranteed by the gain setting procedure (where the decay of the ^{137}Cs γ-source is taken into account). The observed variation, with an overall RMS spread of 1.1 % for barrel modules and 1.2 % for extended barrel modules, is partially due to differences in the

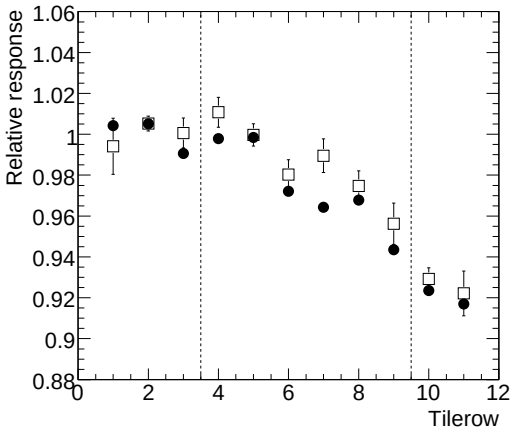

Fig. 27. The average response of muons (full circles) and electrons (open squares) entering the calorimeter at 90°. The results are corrected by the Cs source signal in each tile-row segment, and are normalized to their means in the first three tile-rows. The error bars represent the errors on the mean values. The results involve data from eight (muons) and three (electrons) barrel modules respectively.

calibration procedures over the three years.

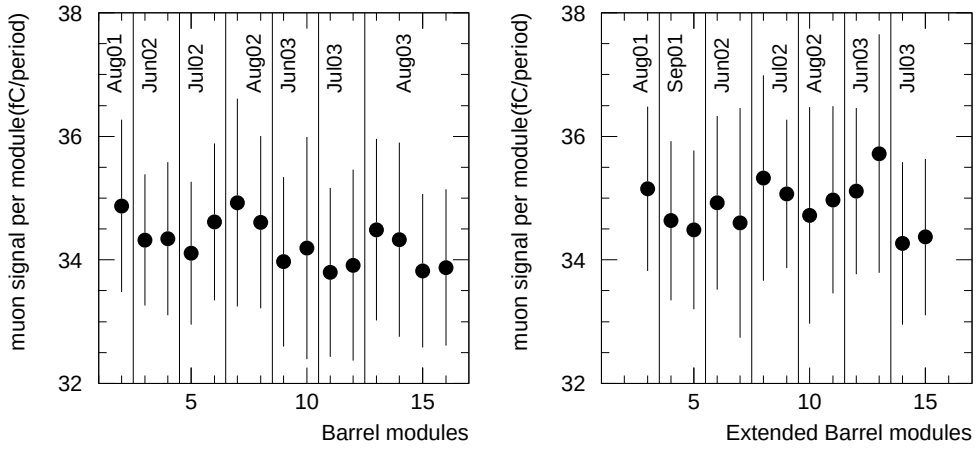

Fig. 28. Average signal per module from muons incident at $\theta_{\mathrm{TB}} = 90°$. The error bars represent the spread of the response over the tile-row segments of a given module. The left plot is for barrel modules, the right plot for extended barrel modules.

4.3.4 Response to muons incident at projective angles

In ATLAS the muon spectrometer is designed to measure muon momenta above 3 GeV/c. Muons will lose a fraction of their energy in the materials preceding the muon spectrometer, particularly in the calorimeters. Bremsstrahlung, pair production and energetic δ-rays typically produce large fluctuations in the energy losses of muons in heavy materials, particularly in the high-energy region of interest at the LHC. For muons sufficiently isolated

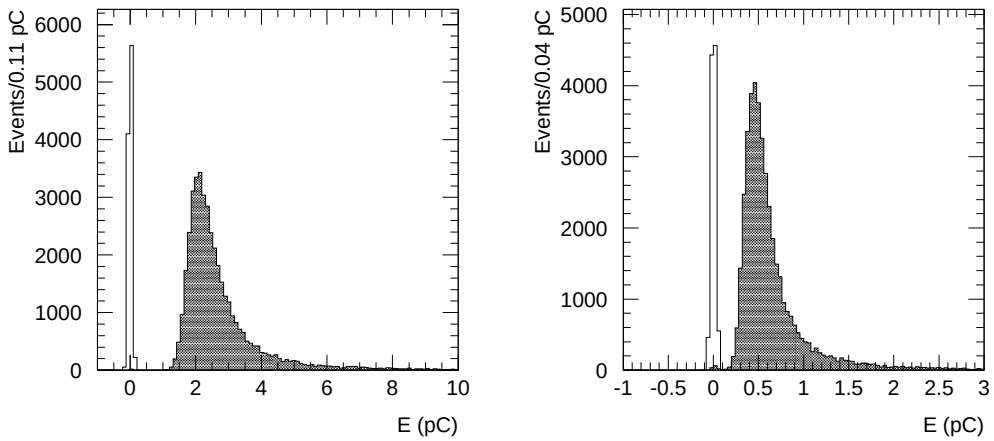

Fig. 29. Example of the isolated muon signal as measured at $\eta = 0.35$ in the whole tower (left) and in the last radial compartment (right). The narrow peaks represent the corresponding noise.

from other activity in the calorimeter, the actual energy loss can be measured and a correction applied. Thus a knowledge of the calorimeter response to muons, as a function of pseudorapidity, is important. The muon test beam data at projective angles are useful for this purpose. Furthermore, results on the calorimeter nonuniformity can be introduced into Monte Carlo simulations of the calorimeter response to other particles or to jets.

An example of the isolated muon signal is shown in Fig. 29 both for the whole tower and the last radial compartment that may be used to tag muons inside jets, because in this compartment hadronic activity will be low [2]. The signal is very well separated from the noise, the signal-to-noise ratio (S/N) being ~ 44 and ~ 18 respectively. [17]

The uniformity of the calorimeter response to muons as a function of pseudorapidity was studied using test beam data from the years 2002 and 2003. The muon beams point to the center of each calorimeter tower and span the η values from -1.45 to 1.35 in steps of 0.1, except for a few points that were either inaccessible due to limitations in the range of the module support table or did not correspond exactly to the future ATLAS setup. [18] The distributions summarizing the uniformity studies in the projective orientation of the calorimeter modules are shown in Fig. 30. The overall spread of the muon response in projective geometry is 2.5 %, demonstrating good uniformity in the construction of the calorimeter modules [30] and in treatment of the calorime-

[17] Because of other constraints the muon signals available to the LVL1 trigger have a poorer signal-to-noise ratio.

[18] Pseudorapidities in the transition region between barrel and extended barrel. In these cases, muons will cross both calorimeter parts in ATLAS setup, but this was never the case in the test beam.

ter signals. Superimposed in Fig. 30 are the MC results, that are in reasonable agreement with experimental data. Bigger differences are observed in the extended barrel. Since muon tracks exit the extended barrel module on its side (see also Fig. 3), the muon path length is more sensitive to the actual beam impact point. The absolute coordinate in the horizontal direction is known only with limited precision (order of 1 cm).

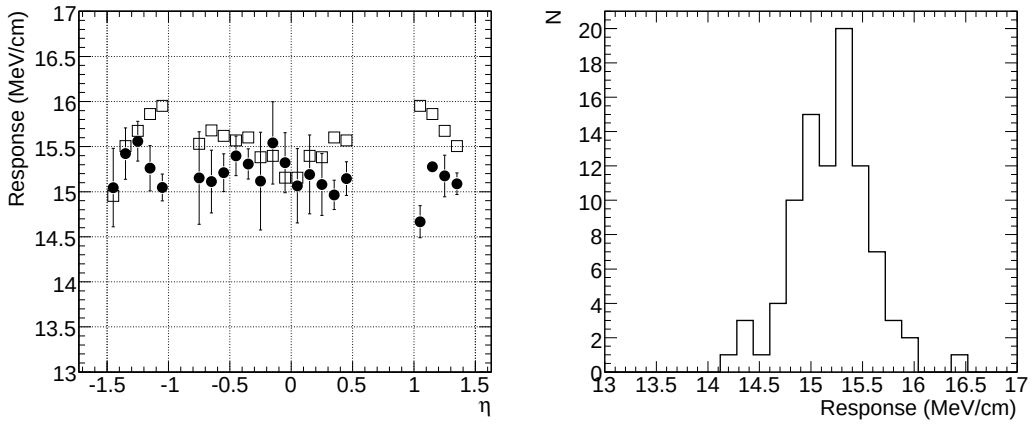

Fig. 30. Left: Average muon signal for projective tracks (full circles), corrected for the variation of muon track length with η and normalized to the muon path length, versus pseudorapidity. This normalization allows direct comparison with measurements at 90°. The error bars represent the spread over all analyzed data for each value of pseudorapidity. Open squares denote the MC results. Right: Distribution of normalized muon signals for 91 projective muon runs. The RMS spread is 2.5 %.

The applied EM scale includes the overall scale factor 1.05 pC/GeV and the correction factors in radial compartments described above. Both data and MC results in Fig. 30 include the e/μ ratio of 0.91 measured with earlier TileCal modules [24]. The average dE/dx for 180 GeV muons in TileCal amounts to 15.2 MeV/cm, as shown in the right panel of Fig. 30.

4.3.5 Response to very low energy muons at 90° *incidence*

Besides providing measurements of the jet and isolated hadron energies, the ATLAS hadronic calorimeter system must help in muon identification, particularly below 3 GeV. Muon test beams with momenta below 3 GeV/c were not available. For this reason, it was deemed useful to perform detailed comparisons of the lowest-energy obtainable muon data with Monte Carlo simulations, in order to gain confidence in further simulations of calorimeter performance for muons of even lower energies.

Decay muons from low energy hadron beams of 3, 5 and 9 GeV, incident at $\theta_{\mathrm{TB}} = 90°$, were used to compare the response to low energy muons with that of a GEANT4-based simulation. The muons had either the nominal beam energy

or an energy from a spectrum extending up to the nominal beam energy, if they were produced from pion decays after the momentum defining magnets. After appropriate muon selection, the distribution of muons ranging out in the calorimeter was fitted to a mixture of the simulated primary and decay muon momentum spectra, leaving the mixing ratio as the only free parameter of the fit [38]. The data and the simulated distributions are compared in Fig. 31.

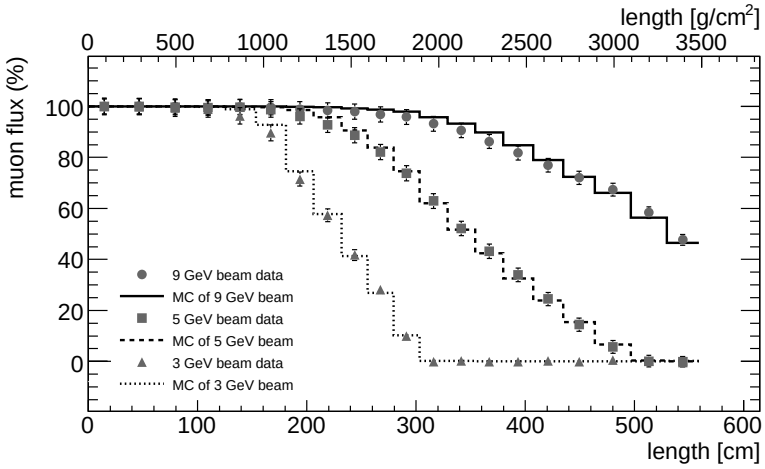

Fig. 31. Fluxes of muons from pion beams with nominal energies of 3, 5, and 9 GeV inside the calorimeter volume in the $\theta_{\mathrm{TB}} = 90^{\circ}$ layout compared to GEANT4 MC simulation. The bin widths correspond to lengths of individual cells.

Independently of the fit to the experimental range distributions, the ratio of the muon flux entering the test beam setup to that from the pion in-flight decays was calculated, based on the known distance from the pion target to the calorimeter module and on the measured rates of pions in TileCal. The two ratios were found to be in agreement, indicating good accuracy of the simulation of the calorimeter response to low energy muons. More details can be found in Ref. [38].

4.4 Results with hadrons

The defining role of hadron calorimetry is to measure the energies of jets. For this purpose, its performance for isolated hadrons is a necessary starting point and is the subject of this section. The hadron selection criteria, pion/proton separation and energy reconstruction methods are discussed in this section. The uniformity of response vs. eta and the variation of response from module to module are analyzed.

The study of pion response and resolution versus energy – the central issue of this section – is then addressed. In the final subsection the response difference between pions and protons is studied.

Results shown here are from data with the beam impinging on barrel modules in the central position of the 3-layer stack used in the test beam. The configuration is shown in Fig. 4. Because of the transverse momenta characterizing hadronic interactions, beam particles entering the top or bottom modules would produce showers which suffer significant transverse leakage.

4.4.1 Event selection

The available data sets fall into two categories: hadron runs, with negligible electron contamination, and electron runs, which contain comparable numbers of electrons and hadrons. In the latter the hadron sample was selected by a cut based on the energy density as defined in Ref. [39]

$$\mathrm{AvD} = \frac{1}{N_{\mathrm{cell}}} \sum_{i=1}^{N_{\mathrm{cell}}} \frac{E_i}{V_i}. \tag{17}$$

Here E_i denotes the energy detected in cell i and V_i is the corresponding cell volume. An entry is made to the sum when the energy in a cell is greater than a specified threshold. In this case 0.06 pC is used, which corresponds to three times the RMS noise in a cell.

The energy density of hadronic showers is typically smaller than that of EM showers. The separation power of a cut based only on energy density grows with the beam energy and is fully sufficient for secondary beams of energy 50 GeV and greater. For tertiary beams (10, 20 GeV) a Cherenkov counter is used to further improve the electron/pion separation. An example showing the most difficult case is given in Fig. 32. Pions are clustered in the bottom-left corner, while electrons occupy the upper-right region. The region with high AvD and pedestal-like Cherenkov signal contains electrons (due to the relatively low efficiency of the Cherenkov counter), but also some pions with anomalously high energy density. The loss of these events is checked with nominal pion runs and appropriate corrections to the total mean response are applied. Nevertheless, this correction is small, never exceeding 0.5 %.

When applying these cuts, the contamination of electrons in the hadron sample is kept below 0.5 % at all hadron beam energies.

The composition of the SPS hadron beams depends on the beam polarity. While negative hadron beams contain mostly pions,[19] positive beams contain a significant number of protons. In the available data set the 50, 100 and 180 GeV hadron beams are positive, and a Cherenkov counter is used to separate pions from protons in many but not all the runs. Typical Cherenkov

[19] Apart from electrons and muons, the admixture of kaons does not exceed 5 % and is neglected.

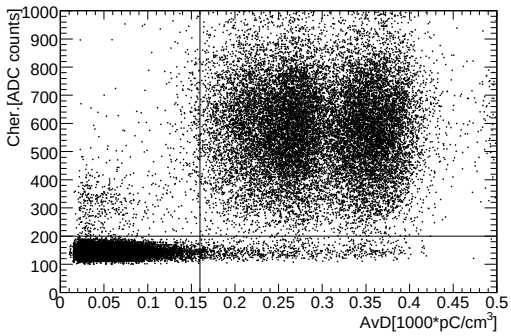

Fig. 32. Scatter plot of the Cherenkov counter signal versus average energy energy density in the calorimeter, for a 20 GeV electron run taken at $\eta = -0.35$. The plot demonstrates the electron/pion separation. Pions are densely clustered in the lower left quadrant and electrons in the upper right. The energy density for electrons is split into two main regions corresponding to two or three cells above threshold in the sum for AvD defined in Eq. (17).

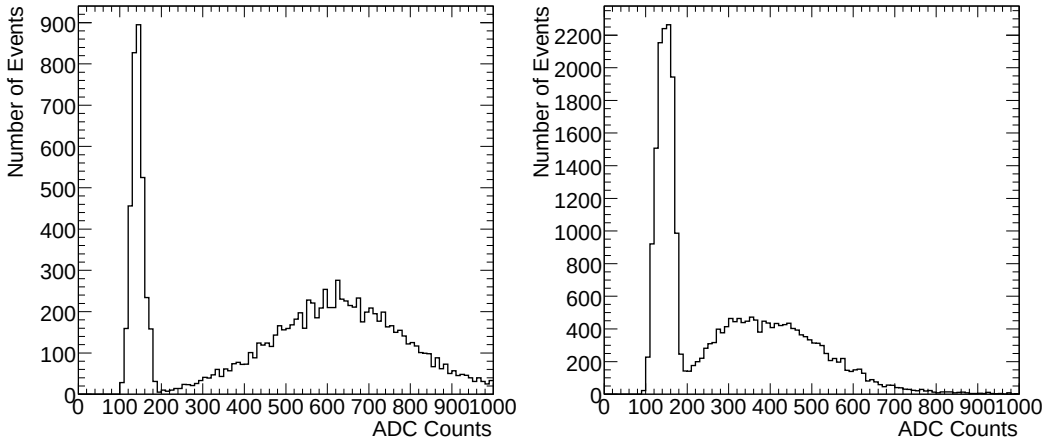

Fig. 33. Two typical Cherenkov counter spectra, for a 50 GeV (left) and a 180 GeV (right) hadron beam. The narrow pedestal peak on the left corresponds to protons, the broad signal on the right to pions.

counter spectra at 50 and 180 GeV are shown in Fig. 33. In the results given below, particles in the mixed positive beams are referred to as hadrons while particles in the negative or Cherenkov-separated beams are referred to as pions or protons.

4.4.2 Reconstruction of hadron energy

For all hadron beam data, the signal from each PMT is calculated using the fit method described in Section 2.2. As illustrated there, the noise with the fit method is about a factor of two lower than with the flat filter method and the signal offset is negligible. Furthermore, it is shown in Section 4.2.3 that the energy resolution for electrons with the fit method is equal or better than

obtained with the flat filter at all energies. This difference cannot be seen with pions, because the coarser pion energy resolution hides the difference between the two methods.

It was also checked that the optimal filter method (Section 2.3) gives the same result as the fit method, within errors. In the low-noise environment of the test beam the numerical outputs of the two methods are almost undistinguishable.

The hadron response is reconstructed by summing the signals from cells of a 3×3 tower matrix, where each tower spans $\Delta\eta \times \Delta\phi = 0.1 \times 0.1$. The matrix is centered on the cell hit by the beam, and corresponds to a cone of a radius $R \approx 0.2$. [20] This energy sum is systematically smaller than that of all cells of all modules in a stack. An appropriate transverse leakage correction is thus applied to the measured mean response shown in Section 4.4.4. No correction is needed for the fractional energy resolution, that is observed to be almost entirely independent of the energy summing method.

Hadron energies are reconstructed at the EM scale, i.e. using one global calibration factor $C_{\mathrm{e}} = 1.05$ pC/GeV obtained from electron data at 20° (see Section 4.2.4) and applying additional calibration factors to the individual radial compartments as obtained with muons at 90° (see Section 4.3.2).

An example of the response to 180 GeV pions impinging on the calorimeter at $\eta = 0.35$ is given in Fig. 34. The calorimeter response is extracted as the peak value of a Gaussian fitted in the range $\pm 2\sigma$ centered around the peak. Response values given below are determined in this way.

The response to hadron-induced showers does not display a significant dependence on the particle's impact point along the z-coordinate (horizontal line perpendicular to the beams). This is unlike electrons showers, whose response must be corrected as shown in Section 4.2.2. This is because the much greater transverse spread of hadron showers averages out local sampling fraction variations, even for small pseudorapidities. Hence no such correction was applied to the data analyzed in this section.

4.4.3 Response uniformity

The module-to-module uniformity of response was investigated using data with a positive polarity beam of 180 GeV. At this beam energy data were taken with most modules, however the Cherenkov counter was not always operational. In order to have a larger and homogeneous data set for studying module response uniformity, no pion/proton separation was performed.

[20] The radius is defined as $R = \sqrt{\Delta\eta^2 + \Delta\phi^2}$.

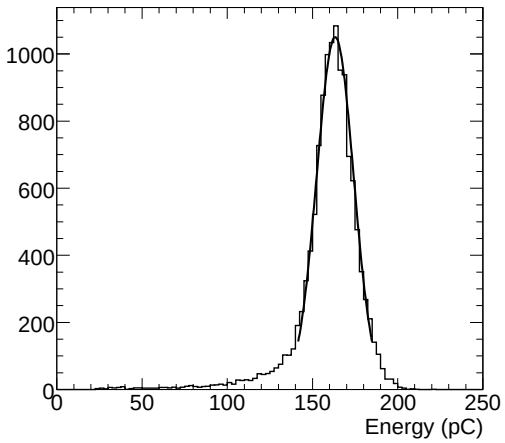

Fig. 34. An example of the response to 180 GeV pions impinging on the calorimeter at $\eta = 0.35$. Also shown is the Gaussian fit performed in the range $\pm 2\sigma$ centered around the peak. The low-energy tail is due to longitudinal energy leakage. It will be less important in the ATLAS configuration where the electromagnetic calorimeter is in front of TileCal.

Figure 35, left, shows the spread in the mean responses of nine modules for a hadron beam incident at $\eta = 0.35$. The RMS variation is $(1.5 \pm 0.4)\,\%$. This is less than the $2.4\,\%$ spread found for electrons at the same angle of incidence ($\theta_{\mathrm{TB}} = 20^{\circ}$), as described in Section 4.2.4. Since hadron showers populate more calorimeter cells, variations in the response of individual cells is reduced by the averaging process and the response is more uniform. The uniformity was also investigated at different pseudorapidities as demonstrated in Fig. 35, right. The results obtained show that the uniformity of the response is independent of pseudorapidity, within errors. The mean of the RMS variations between modules at different pseudorapidities is $(1.4 \pm 0.2)\,\%$.

The response to hadrons and the fractional energy resolution as a function of pseudorapidity are shown in Fig. 36. These results were obtained with a setup in which a production barrel module was placed above the central barrel module, instead of the two extended barrel modules shown in Fig. 4. This eliminated the transverse leakage present in the usual setup for incidence at small pseudorapidities.

The measured responses in Fig. 36 (left) are slightly lower at small pseudorapidities due to longitudinal leakage. The open circles show the results of correcting for this effect using measurements in the 90° configuration [40]. The lower response at $|\eta| = 0.75$ is due to transverse leakage. The errors are taken to be $1.4\,\%$, as shown in Fig. 35. Excluding the point at $|\eta| = 0.75$, the response corrected for longitudinal leakage has an RMS spread of $0.6\,\%$.

The energy resolution as a function of pseudorapidity is shown in Fig. 36 (right). As expected, it is significantly worse where longitudinal leakage is

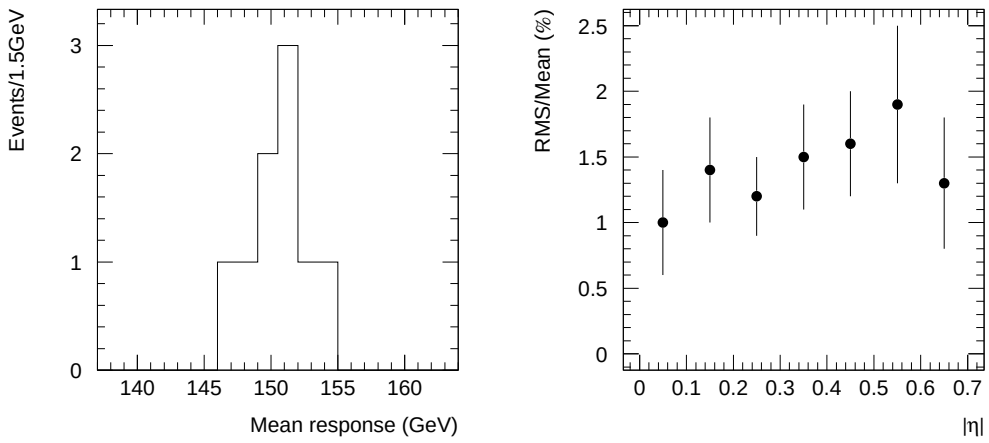

Fig. 35. Left panel: the module-to-module uniformity as obtained with 180 GeV hadrons, incident at $|\eta| = 0.35$. The RMS spread in response is $(1.5 \pm 0.4)\,\%$. The right panel shows the RMS variation between modules as a function of $|\eta|$. It has an average value of $(1.4 \pm 0.2)\,\%$. In both plots $\pm\eta$ symmetry is assumed.

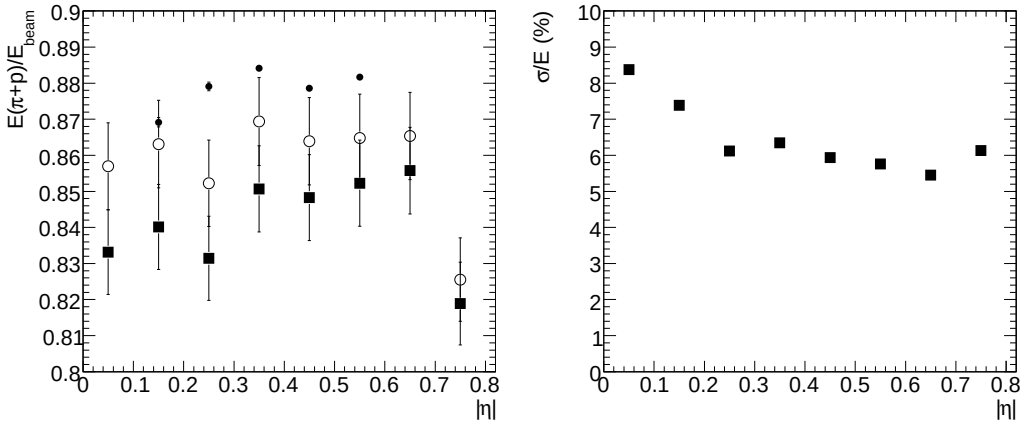

Fig. 36. The mean reconstructed energy (left) and resolution (right) for 180 GeV hadrons incident at various pseudorapidities. Full squares denote the data. The open and small full circles represent data and GEANT4 MC simulations respectively, after applying the longitudinal leakage corrections from [40]. In the right panel the statistical errors are smaller than symbols used.

larger, but it appears to be only insignificantly affected by transverse leakage at $|\eta| = 0.75$.

4.4.4 Pion response versus energy

In this section, the pion response is defined as the ratio of the reconstructed pion energy to the beam energy. As the pion energy is calculated applying the charge-to-energy conversion factor measured with electrons (see Section 4.4.2), the pion response is identical to the ratio of responses for pions and electrons,

also known as the π/e ratio. In a non-compensating calorimeter like TileCal, this ratio is expected to rise slowly with pion energy.

Hadron data taken with TileCal production modules do not provide a broad energy scan in any single module; instead, data taken with any particular module typically span only two or three energies. Therefore when studying the response to hadrons as a function of particle energy the module-to-module variation of 1.5 % (see Section 4.4.3) partially obscures the variation with energy. This problem can be alleviated by exploiting the fact that most module energy scans include a point at 180 GeV and $|\eta| = 0.35$. This allows a normalization of all modules to a common response at this energy and angle of incidence. When this is done a smoother series of response values is obtained, comprising 6 values of the beam energy, from 10 GeV to 350 GeV.

All available pion results at $|\eta| = 0.35$ are summarized in Fig. 37 and in Table 4. The responses are first plotted in the left panel without leakage corrections, for comparison with Monte Carlo simulations, and then with longitudinal and transverse leakage corrections, in the right panel of Fig. 37, for further analysis. The simulation results in the Table were obtained with the GEANT4 version and physics models mentioned in the introduction of Section 4. They are in reasonably good agreement with the experimental results.

The longitudinal leakage correction factors given in the Table were obtained from the measurements of Ref. [40]. Transverse leakage corrections are also necessary, in particular because the pion response is summed from cells of a cone size $R \approx 0.2$ (see Section 4.4.2). Two sets of transverse leakage corrections were calculated: from the GEANT4 simulations just mentioned, and from a study of transverse leakage on data from an earlier generation of TileCal modules [41]. The GEANT4 simulations are known to underestimate the transverse leakage fractions [40], whereas the latter studies may be an overestimate because of the greater radial depth of the prototype modules. The averages of the two correction factors thus obtained were used to correct the responses for each beam energy.

After normalizing the response of each module at each energy to the common response at 180 GeV, the remaining error on each single response measurement is estimated to be 1 %. It mostly arises from variations in local module response, uncertainties in the charge injection calibration and the cesium calibration. This error is combined in quadrature with the uncertainty in the beam energy. A systematic error equal to one-half the difference between the two sets of transverse leakage correction factors may be taken as a lower limit to the systematic error on the response. Finally, the overall scale of the response may be affected at the $1 - 2$ % level by further error sources – for instance, from the uncertainty in the response to the electromagnetic component of the hadron shower.

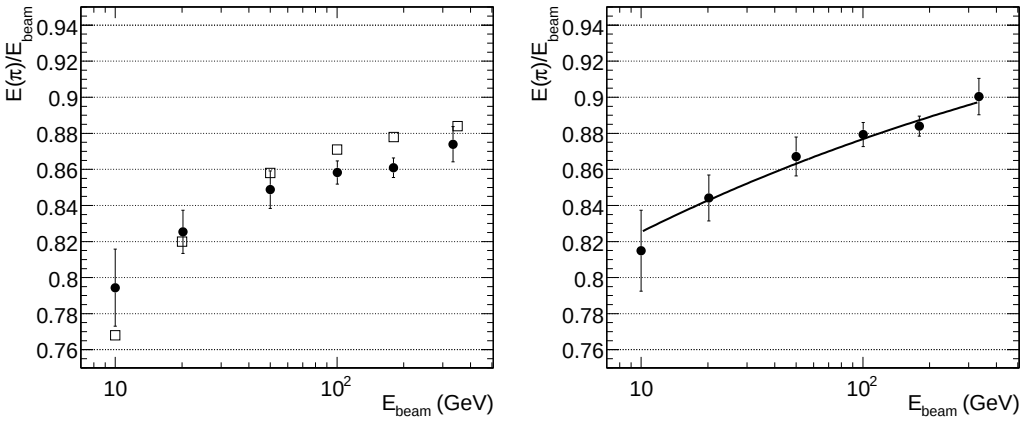

Fig. 37. Pion response vs. energy of incident pions at $\eta = 0.35$. Left panel: experimental data (full circles), where the responses in every module are normalized to each other at 180 GeV. Open squares represent GEANT4 Monte Carlo simulations. Right panel: the same experimental data corrected for longitudinal and transverse energy leakage, as described in the text. The line shows the fit to Eq. (19) with the parameter values given in the text.

			Leakage corrections		
E_{beam}	$E(\pi)/E_{\mathrm{beam}}$		Longitudinal	Transverse	
(GeV)	Data	GEANT4		GEANT4	Prototypes
10	0.794 ± 0.021	0.768 ± 0.002	1.008	1.012	1.023
20	0.825 ± 0.012	0.820 ± 0.002	1.011	1.008	1.016
50	0.849 ± 0.010	0.858 ± 0.002	1.014	1.006	1.011
100	0.858 ± 0.006	0.871 ± 0.001	1.017	1.006	1.008
180	0.861 ± 0.005	0.878 ± 0.001	1.021	1.005	1.006
350	0.874 ± 0.010	0.884 ± 0.001	1.026	1.004	1.004

Table 4
The pion response relative to the beam energy $E(\pi)/E_{\mathrm{beam}}$, where the responses of every module are normalized to each other at 180 GeV. Also given is the prediction by GEANT4.8.3 MC using the QGSP and Bertini cascade models. The longitudinal leakage corrections are from Ref. [40]. The corrections for transverse energy leakage were obtained from the same GEANT4 MC and from experimental data of an earlier generation of TileCal modules [41].

The corrected pion response may be parametrized and compared with previous measurements. In Groom's parametrization [42,43],

$$F_{\mathrm{h}} = \left(\frac{E_{\mathrm{beam}}}{E_0}\right)^{m-1} \tag{18}$$

F_{h} represents the non-EM energy component of showers induced by incident

hadrons of the energy E_{beam}, E_0 is the energy at which multiple pion production becomes significant, and the parameter m must be determined empirically for a given calorimeter. The pion response then reads

$$\frac{E(\pi)}{E_{\mathrm{beam}}} = (1 - F_{\mathrm{h}}) + F_{\mathrm{h}} \times \left(\frac{\mathrm{e}}{\mathrm{h}}\right)^{-1} \tag{19}$$

where e/h is the usual ratio between the responses to the purely EM and hadronic components of showers. Among the three free parameters of Eq. (19) the value of E_0 was fixed to 1 GeV; the fit to the response shown in Fig. 37 gives the values $\mathrm{e/h} = 1.33 \pm 0.06 \pm 0.02$ and $m = 0.85 \pm 0.03 \pm 0.01$, where the first error is statistical and the second corresponds to the systematic error on the transverse leakage corrections. These errors do not display the correlation between e/h and m.

Fitting to the data another commonly used parametrization of the hadronic fraction, $F_{\mathrm{h}} = 1 - 0.11 \log(E_{\mathrm{beam}}/E_0)$, with $E_0 = 1$ GeV, $\mathrm{e/h} = 1.336 \pm 0.013 \pm 0.005$ is obtained. The values of e/h obtained with these two parametrizations agree within errors.

These results on e/h are in agreement with earlier TileCal measurements [3,44]. A similar value was found also for the CDF end-plug calorimeter [43], which however has a different sampling fraction.

Finally, the pion data sets used to obtain the response are also used to measure the fractional resolution as a function of energy. The values are shown in Fig. 38 and are compared there with GEANT4 simulations. The two are in good agreement. The experimental resolution is well-represented by the parametrization of Eq. (16), with $a = (52.9 \pm 0.9)\,\%/\mathrm{GeV}^{1/2}$, $b = (5.7 \pm 0.2)\,\%$. The noise contribution appears negligible at all energies, therefore no such term was considered in the fit. This result is also in a good agreement with energy resolution measured with TileCal prototype modules, after accounting for the $1.5\lambda_{\mathrm{int}}$ additional depth of the prototype calorimeter modules [45]. It also represents a more complete analysis of the data reported in Ref. [1] and supersedes that result.

4.4.5 Pion/proton response ratio

As already mentioned in Section 4.4.1, beams of positive polarity contain significant fractions of protons, ranging from 32 % at 50 GeV to 76 % at 180 GeV. Therefore, a special study of the difference between pion and proton responses was carried out.

The measured response ratio π/p is shown in Fig. 39 (left), where the ratio is seen to fall towards unity with increasing energy. Figure 39 (right) shows the

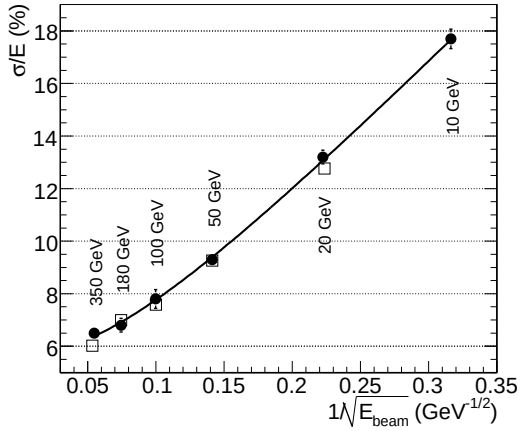

Fig. 38. The fractional energy resolution for pions at $\eta = 0.35$ as a function of incident energy. Experimental data (full circles) and GEANT4 simulations (open squares) are in reasonably good agreement. The data are fitted with the usual formula (16) as described in the text.

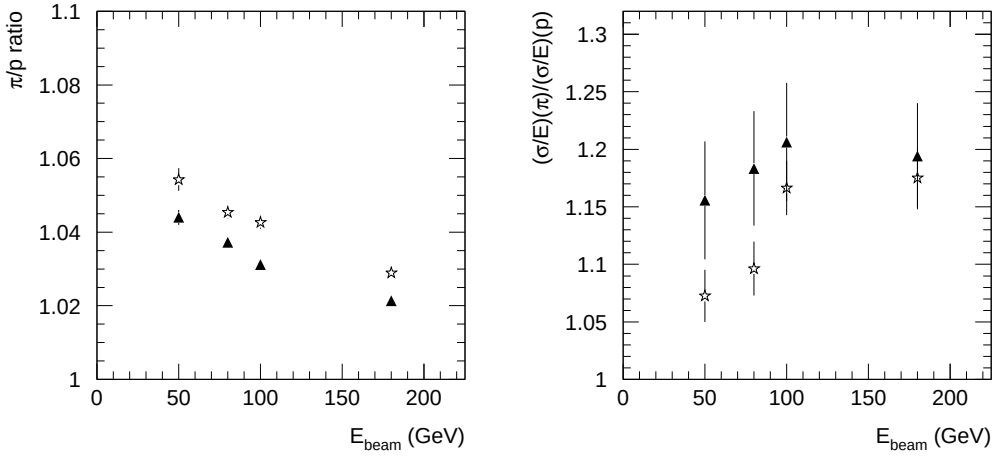

Fig. 39. The energy dependence of the π/p ratio (left) and ratio of the energy resolutions for pions/protons (right) as measured at $\eta = -0.35$. Experimental data are shown with full triangles, the GEANT4 MC simulations (version 5.2, with the QGSP model) are represented by stars.

ratio of resolutions and indicates $15-20\,\%$ better resolution for protons in the range of energies studied. Also given are the results of a GEANT4 MC simulation. It should be noted that an older version (5.2) of GEANT4 was used for these studies. It contains the QGSP model for hadronic interactions but without the Bertini intranuclear cascade model. Nevertheless it still reproduces the slow decrease with energy. The π/p values appear to be independent of pseudorapidity in the calorimeter as demonstrated in earlier test beam measurements [46].

Response values $\pi/\mathrm{p} > 1$ imply a lower hadronic component fraction F_h (see

Section 4.4.4) for pions than for protons. This is also predicted by MC simulation [42]. The better energy resolution for protons corresponds to smaller fluctuations in the energy deposition mechanism for protons. Both this effect and the reduced signal for protons are understood in terms of leading particle effects as proposed in Ref. [31].

5 Summary and Conclusions

The results described in this paper characterize most aspects of the performance of the ATLAS Tile Calorimeter. They were obtained in the well-controlled test beam environment from a representative sample of the modules that compose it and will provide a useful reference for the performance of TileCal in the LHC environment.

Conclusions from the module test program may be divided into two categories: general system properties, and response to particle beams. The general properties will be addressed first.

By reconstructing the energy in each PMT by the fit method described above it is found that the electronic noise is about 20 MeV (RMS value), or about 1.3 ADC channels. An optimal filtering method will be used in the colliding beam environment, where minimum bias events will give a more significant noise contribution.

With the system's dynamic range of about 10^5 the low-end signals from isolated muons are well separated from noise even in the worse cases. The high end of the ADC scale is equivalent to 1.5 TeV/cell. Considering jet shapes and the longitudinal and transverse spread of hadronic showers such an energy deposition limit should be exceeded at most only a few times a year at design luminosity. In such rare but possibly very interesting cases of saturation, signal recovery is possible up to at least 2.2 TeV/cell, as shown in the Appendix A.3.

The overall response of the calorimeter and of its readout chain is calibrated by means of several monitoring systems, designed to characterize the response at various points on the path of the signal from the scintillators to the digitized particle signals. Specifically,

(1) A charge injection system (CIS) reconstructs the PMT signal's charge, calibrating away the spread in channel gains and the small non-linearities in the signal processing chain from the PM anode onwards.
(2) A laser system delivers light pulses that span the dynamic range of all the 9344 TileCal PMTs, characterizing gain and any deviations from

linearity.

(3) A hydraulic system moves a ^{137}Cs γ-ray source through the calorimeter modules and precisely measures the scintillation light produced in each of the approximately 420,000 scintillating tiles. This very detailed 3D map of the entire calorimeter is obtained by measuring the time-averaged PMT currents by a separate electronic chain, and is initially used in setting the PMT gains to obtain equal responses in all readout cells.

(4) The source readout electronics will be used in the LHC environment to measure the currents associated to the minimum bias collisions, thereby providing an online monitor of the behaviour of each cell.

The stability and maintainability of cell inter-calibrations are as important as the attained precision. Charge injection measurements of front-end electronics gains have been shown to be stable within 0.2 % (RMS) over four months; the deviations from the initial settings with the Cs system have an RMS spread of 0.2 % over one month, and 0.9 % over 4 months; laser runs over month-long periods are not available yet, however runs over few days show that gains can be monitored with better than 0.5 % accuracy. These drifts can all be monitored, and corrected when necessary.

Data taken with beams of electrons, muons and hadrons measure important physics response parameters while complementing results obtained with calibration runs. For instance, electron data show that the best energy resolution is obtained by reconstructing the signal with the fit method.

The main use of electron data is to set the charge-to-energy conversion factor for electromagnetic showers – the *electromagnetic scale factor* – which is the starting point to measure the response to hadrons. In order to properly measure this basic parameter a number of effects intrinsic to the TileCal design must be taken into account. First, the periodic scintillator/iron plate structure determines a characteristic variation of the signal with the electron's point of incidence, which must be corrected using position information. Second, the same structure causes a variation of the response with the angle of incidence. To avoid this latter cause of signal spread, electrons are measured always at the same angle of incidence to the module face ($20^\circ, \eta = 0.35$).

The electron response thus measured on about 200 cells has an RMS spread of 2.4 % which is understood to originate mostly from local optical variations at the level of individual tiles and tile/fiber couplings. Inserting these local responses, measured with the Cs source, into GEANT4 simulations this spread is reproduced. The mean value of the EM scale factor is 1.050 ± 0.003 pC/GeV.

This measurement only characterizes the response of the cells of first radial compartment of TileCal (the A-cells) because the EM shower is almost entirely absorbed in these cells. Measuring the EM scale factor in the other compart-

ments is accomplished in part using electrons at 90°, which penetrate only the cells at the edge of the modules.

The local response variations just mentioned do not allow a precisions of better than ±3 % in measuring the linearity of electron response vs. energy. The energy resolution is parametrized by the sum in quadrature of a statistical term (28 % $\mathrm{GeV}^{-1/2}$) and a constant term of 2.8 %, to which the local nonuniformities clearly contribute.

It should be stressed that the response variations seen with electrons do not affect the intended use of the Tile Calorimeter for ATLAS physics, because electromagnetic showers are almost entirely absorbed in the liquid argon EM calorimeter upstream of TileCal.

Data with 180 GeV muons at 90° incidence were taken on all modules, centering the beam on each of the 11 tile-rows of each module. These detailed scans allowed precise measurements of the EM response throughout the volume of modules. It was found that the cell response equalization obtained with the Cs source signals had to be corrected in the second and third radial compartments (BC, D cells and B, D cells in the barrel and extended barrel modules respectively). This effect is due to a variation of scintillation light yield of tiles along their radial axis. The variation with tile-row number of the response to 90° muons is in good agreement with the variation measured with electrons. This correction (1 % – 8 %) will also be applied in ATLAS.

Muon run results can be examined at the level of individual tile-row segment responses, and can be further refined by intercalibrating them with the Cs source data at the same granularity level. The resulting muon responses are found to be in good agreement with 90° electron responses over the 11 tile-rows, which gives a useful consistency check of the procedure used to extract the EM scale factor. Additional results from 90° muon runs include the average responses of all exposed modules over four years of test beam data, which have an RMS spread of 1.1 % (1.2 %) for (extended) barrel modules.

In projective geometry, the signal/noise ratio of the muon signals at $\eta = 0.35$ is about 44 in the entire tower and about 18 in the last radial compartment. Over an η range of ±1.5, the RMS spread of the signal from the whole tower is 2.5 %. Projective muons give information about the radial dependence of the uncorrected signal consistent with that from 90° electrons and muons.

Hadron response was studied over the energy range from 10 GeV to 350 GeV, with positive or negative charge beams. With the former, protons constitute a significant fraction of the incident particles; in these cases, pions and protons were separated using a Cherenkov counter. In projective geometry, the modules are not deep enough to contain the entire hadron shower, and corrections for longitudinal leakage had to be applied. The hadron signal was

reconstructed applying the EM scale factor, with no correction. Signals from the three radial compartments were added, over a 3×3 matrix of towers, centered on the cell hit by the beam.

Studies of the uniformity of hadron response within and between modules mostly used 180 GeV beams. The response vs. η, after correcting for longitudinal leakage, has an RMS spread of 0.6 % over $0 < \eta < 0.7$. The response at $\eta = 0.35$, measured on 9 modules, has an RMS spread of (1.5 ± 0.4) %, which can be compared to the analogous figure for electrons, (2.4 ± 0.1) %.

The response with energy of the three-module stack exposed to hadrons is the main result of the studies reported here, because it will apply to the reconstruction of the energy of jets in ATLAS. Results are obtained for hadrons incident at $\eta = 0.35$, and combining data from several modules, as explained earlier. The response, given in terms of the ratio of the measured energy (on the EM scale) to the beam energy, shows the typical behaviour of a non-compensating calorimeter, as expected. It is fitted with Groom's parametrization of hadronic response, yielding an e/h $= 1.356 \pm 0.013$, in agreement with previous TileCal results and in line with expectations. The resolution as a function of energy is parametrized with a statistical term of $(52.9 \pm 0.9)\,\%/\mathrm{GeV}^{1/2}$ and a constant term of (5.7 ± 0.2) %. The latter term is affected by incomplete shower containment.

The difference between the responses of pions and protons was studied from 50 GeV to 180 GeV. The pion/proton signal ratio varies between 1.05 and 1.02 over this range. Energy resolutions for protons are 1 % to 2 % better for protons than for pions, consistent with expectations from a smaller EM component in proton-initiated showers. This is one of very few experimental results on this issue.

In concluding this paper it is worth to remark that from the data of the TileCal test beam program some results of general physics interest have been obtained. These results provide precision measurement of the radiative energy losses of high-energy muons [47] and on muon photonuclear interactions [48].

Acknowledgements

We sincerely thank the technical staffs of the collaborating Institutes for their important and timely contributions. Financial support is acknowledged from the funding agencies of the collaborating Institutes. We are grateful to the staff of the SPS, and in particular to K. Elsener and A. Fabich for the excellent beam conditions and assistance provided during our tests. We thank Nicolas Kerschen for providing the calculations of precise values of the beam energy

settings. We also want to express our gratitude to C. Ferrari and his team for the maintenance of the support scanning table.

We acknowledge the support of Yerevan Physics Institute, Armenia; State Committee on Science & Technologies of the Republic of Belarus; CNPq and FINEP, Brazil; CERN; Ministry of Education, Youth and Sports of the Czech Republic, Ministry of Industry and Trade of the Czech Republic, and Committee for Collaboration of the Czech Republic with CERN; IN2P3-CNRS, France; Georgian Academy of Sciences; GSRT, Greece; INFN, Italy; JINR; GRICES and FCT, Portugal; Ministry of Education, Research and Youth, Romania; Ministry of Education and Science of the Russian Federation, Russian Federal Agency of Science and Innovations, and Russian Federal Agency of Atomic Energy; Department of International Science and Technology Cooperation, Ministry of Education of the Slovak Republic; Ministerio de Ciencia y Innovación, Spain; The Swedish Research Council, The Knut and Alice Wallenberg Foundation, Sweden; DOE and NSF, United States of America.

A Other Studies related to Operation in ATLAS

Particle beams provide a convenient source of signals, which can be used to study several calorimeter performance aspects relevant to operation in the ATLAS environment. This is because signals from different cells have the proper time relationship, and may cover a realistic dynamic range. Some of these studies are reported in this Appendix. They include relative channel timing and recovery of the signal from saturated readout channels. In addition, beam tests allowed to study the performance of an analog tower sum, that will be used to provide the ATLAS first-level trigger. The properties of this signal are also described in this Appendix.

A.1 Analog Trigger Output

As already mentioned in Section 1, the Tile Calorimeter signal also contributes to the first level trigger (LVL-1). The analog low-gain signals from the PMT 3in1 cards enter an adder circuit which provides a fast analog signal corresponding to the total energy in an $\eta \times \phi = 0.1 \times 0.1$ bin, and an amplified signal corresponding to a single PMT in the last radial sampling. [21]

[21] Tagging muons in Tilecal at LVL-1 was considered after the primary electronics design was completed. Since this output originates from the low-gain signal, the discriminating power for small signals such as a single muon is limited. Its role is to be used in conjunction with other muon trigger requirements.

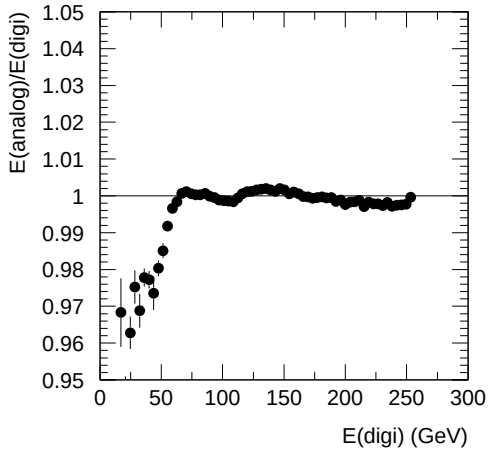

Fig. A.1. The adder tower signal linearity with respect to the digitized energy (sum of the energies from corresponding channels).

The calibration of both kinds of signal is very briefly described. Then, we concentrate on the two main issues:

- linearity and resolution of the trigger tower signal that enters the overall ATLAS calorimeter LVL-1 trigger
- capability of the muon output to assist in the muon identification

More details about the analog adder performance can be found in Refs. [50,51].

The gain measurements for the trigger tower sum (slope of the amplitude with respect to the sum of energies reconstructed using the digitized signals from corresponding PMTs) confirmed the laboratory-measured gain with an RMS spread of 2 % [51]. The measurements also showed that any cross-talk is less than 0.2 %.

The energy linearity and resolution of the tower sum signal affect the performance of the LVL-1 event selection based on jet energy and missing-E_{T}. A linearity better than 1 % for energies $E > 65$ GeV is obtained for the ratio of the the analog tower sum signal to the energy calculated from individual digitized PMT signals. This is shown in Fig. A.1. The testbeam data also show that the energy resolution σ/E in the analog system does not deteriorate by more than 1 % (additional constant term to be add in quadrature to the standard energy resolution) for energies above 80 GeV.

The performance of the muon output was tested using the high-energy muon beams (both η - projective and $\theta_{\mathrm{TB}} = 90^{\circ}$). The gain measurements match the laboratory results. The channel-to-channel variations exhibit an RMS of 1.5 % [51].

The role of the muon output is to assist in muon tagging based on the signal in

the last radial compartment. Therefore, its signal-to-noise (S/N) ratio [22] has been measured using isolated high-energy muons impinging on the calorimeter at different η. The results for the barrel section are shown in Fig. A.2 and correspond to the sum of the two adder muon outputs seeing the same cell. The $S/N = 2.84$ at $\eta = 0.15$ and this translates to an efficiency of $\sim 85\,\%$ with $90\,\%$ noise rejection. In the extended barrel section, $S/N > 5$ because of thicker cells in the radial direction (see Section 1) and longer muon track-length at larger η. When considering only a single muon output (i.e. 1 PMT of the two reading the outer cell), the S/N decreases by $\sqrt{2}$. The efficiency of muon tagging is then $\sim 75\,\%$ ($\eta = 0.15$) for $90\,\%$ noise rejection. The typical RMS noise in a single muon output corresponds to 0.15 GeV.

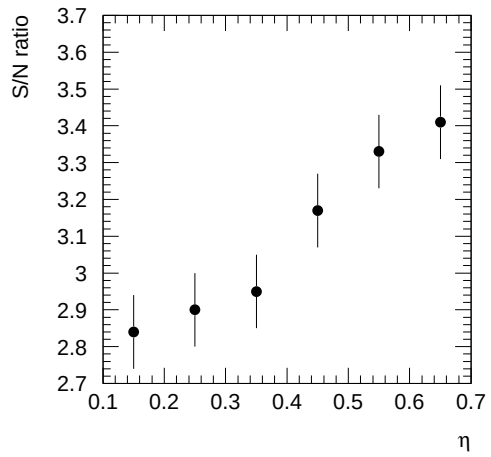

Fig. A.2. The S/N ratio for isolated muon as measured in the adder muon output (Tile calorimeter barrel section). The values correspond to the sum of two adder muon outputs seeing the same cell.

A.2 The Timing of the Tile Calorimeter

The time synchronization between the cells of Tile Calorimeter and the bunch crossing (BC) identification is one of the most important triggering issues. The cells' timing needs to follow the tower projective geometry reflecting the different flight path of the particles in the calorimeter. Global timing will be realized primarily with the beam events but initially adjusted by means of the laser calibration system. As a check on these methods, a bunched beam with 25 ns RF structure was used in the results below.

The laser calibration system can be used for pre-setting the timing of the calorimeter signals [52].

[22] Calculated as the most probable value of the muon signal divided by the noise width (Gaussian sigma).

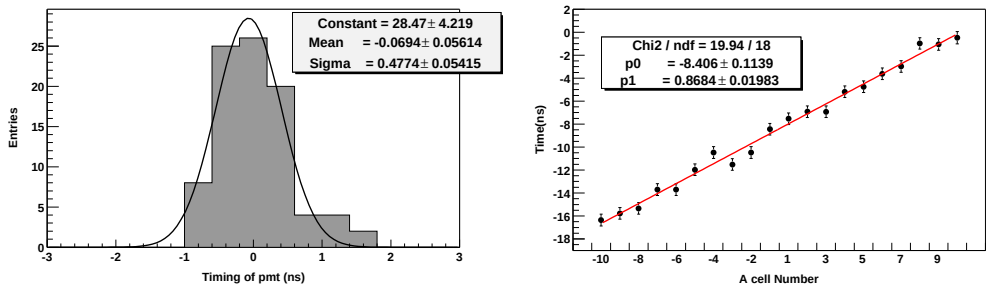

Fig. A.3. On the left, the difference in time between the generic channel and the reference one once the corrections for the delays introduced by the clear fibers inside the module have been taken into account. On the right, the timing of a muon impinging at 90° on the A cells. The slope indicates a value of 31 ± 2 cm/ns for the speed of the muon.

The pulse-to-pulse jitter of the laser output with respect to the trigger is about 30 ns, but this can be eliminated by considering timing with respect to a reference channel. The timing of each channel with respect to the reference PMT is the result of two different factors. First, the difference in length of the clear laser fibers introduces a different PMT-PMT delay. These delays are present only for the laser system and have to be removed. Secondly, there is a delay of the propagation of the TTC signals along the length of the drawer. This can be calculated precisely for any digitizer board once the correction of the laser has been applied. It turns out to be around 2.5 ns for each digitizer board, and it is removed before the checking of the overall timing.

For adjusting the readout times a scan of the timing configuration of the digitizers can be performed by varying a register in the digitizer called DSkew2. Choosing a reference time T_0, it is possible to calculate the DSkew2 value for each channel that corresponds to that T_0. By minimizing the mean square error between the reconstructed time of each channel and the reference time T_0 we see in Fig. A.3 (left plot) that a precision well below 1 ns can be achieved. The right plot of Fig. A.3 shows a cross check of the time setting. Muons impinging at 90° degrees on the A cells have been considered. The timing obtained in each cell has been plotted against the cell number, i.e. the cell position. The slope obtained leads to a measurement of the speed of the muon of 31 ± 2 cm/ns, which confirms the validity of the time settings.

The final determination of the time for each digitizer will be done using particles synchronized with the BC clock of 40 MHz. This was tested during a testbeam period with a 25 ns bunched beam. The beam had a periodic structure with 48 bunches at 25 ns for a total of 1200 ns. The time between a bunch group and the following one was of 23 μs.

The reconstructed time for one channel is shown in Fig. A.4. The distribution on the left refers to low gain events while the one on the right is for events

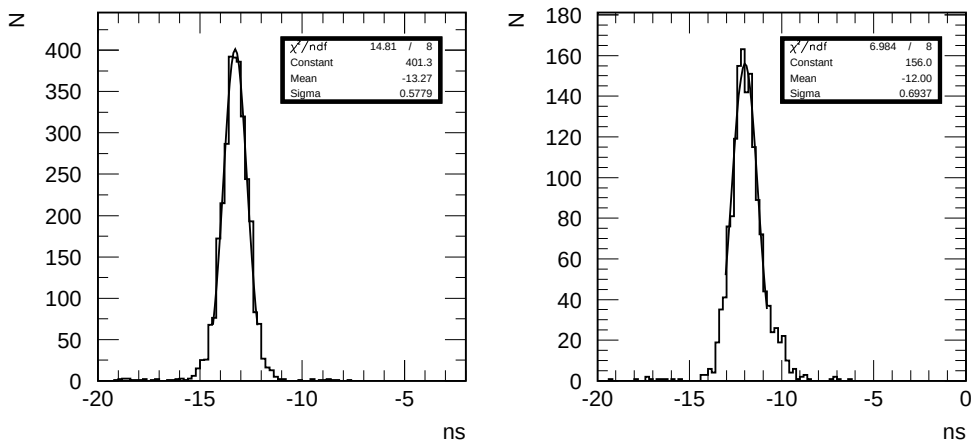

Fig. A.4. Distribution of time for events acquired with low gain (left) and high gain (right).

acquired with high gain. The resolution is well within 1 ns and has been shown in Ref. [53] to approach 200 ps at high energy.

As can be seen in Fig. A.5, the channel-to-channel variation of the timing for each channel has an RMS spread of less than 1 ns. This has also been confirmed by a separate analysis [54]. The comparison between the timing of one channel obtained with the laser and the one obtained with the beam is shown in Fig. A.6. They are the same with a ± 1 ns accuracy.

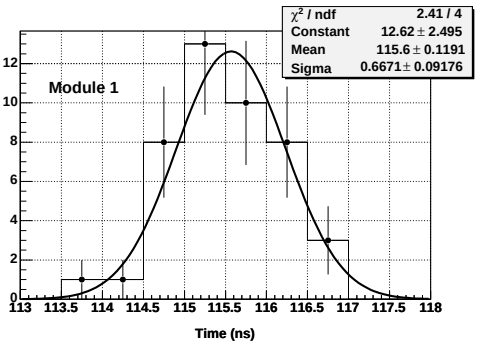

Fig. A.5. Relative signal timing for laser pulses seen by 45 channels in a barrel module after all adjustments to equalize timing.

A.3 Recovery of Electronic Saturation

The dual gain electronics coupled to each photomultiplier allows a measurement of single cell energy deposits ranging from $\simeq$ 100 MeV to $\simeq$ 1.5 TeV. A cell energy deposit greater than $\simeq$ 1.5 TeV saturates one or more of the digitized time samples. Only few such events per year are expected at the nominal luminosity.

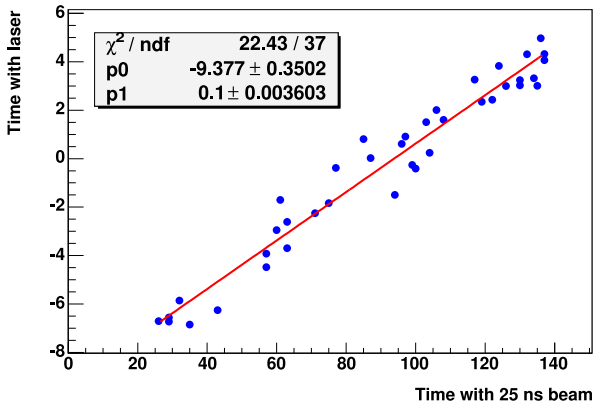

Fig. A.6. Correlation between the time found with the 25 ns beam (one unit = 104 ps) and with laser.

In ATLAS, there is the option of reprocessing such raw data for further analysis. Since the time shape of the signal is fixed by the shaper circuit, the partial information obtained from the time samples that did not reach the saturation limit may be used to infer the cell energy deposit.

Two methods of recovering the original signal are presented:

- The fit method restores the signal keeping the linearity within 3 % provided only one sample saturates (see Section A.3.1). This feature effectively enhances the dynamic range by $\sim$ 50 % and is important for further online data processing in high level trigger.
- Better performance can be reached when applying special treatment offline. As demonstrated in Section A.3.2, the dynamic range can be increased by a factor of two while keeping the linearity within 1 %.

The performances have been studied using both events generated by the charge injection system [55] and with physics triggers [56].

A.3.1 Saturation Recovery Method Applied to Charge Injection System Events

In order to study the performance of the method special runs have been used in which a charge scan is performed over the full range. Data are acquired for each injected charge Q with both gains and with variable injection time. The value of each sample is indicated in the following as s_i with $i = 1 \ldots 9$. The peak time and the peak amplitude depend on the injected time and Q respectively. In order to have the signal independent of time, a sample of CIS events where the charge was injected at a fixed time has been selected.

When the energy is reconstructed with the fit method, the saturation of one sample is almost fully recovered because the fit is performed using unsaturated samples. In Fig. A.7 (left) the reconstructed charge with the fit method is shown as a function of the injected charge for the high gain. The black squares refer to events with no saturated sample, the white squares to those ones with one saturated sample and stars with two saturated samples. The time is not held fixed in this fit reconstruction but for a fixed time and/or pedestal, the linearity for two saturated samples could be better. It can be seen that the loss of one sample is not critical. In Fig. A.7 (right) the ratio between the reconstructed energy and the energy calculated from a linear fit of the part with no saturated samples is shown. The linearity with one saturated sample is within 3 %. However, as more than one sample saturates, the linearity degrades rapidly.

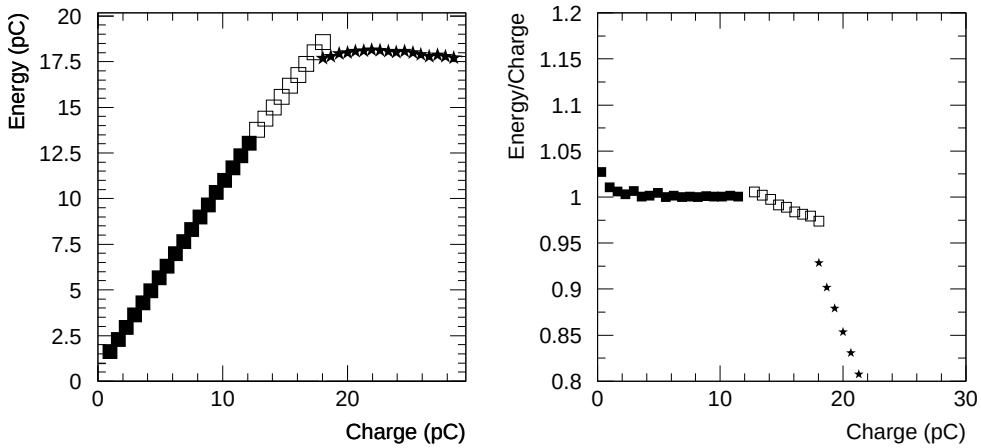

Fig. A.7. On the left, fit method reconstructed charge as a function of injected charge (black squares, no saturated sample; white squares, one saturated sample; stars, two saturated samples). On the right, the ratio between the reconstructed charge and the injected charge. The small non-linearity at very small Q is an artifact of the fit method for CIS events.

In order to recover these events we can exploit the flat filter algorithm. The signal is defined as the quantity S_5 (see also Eq. 1)

$$S_5 = \sum_{i=3}^{7} s_i - 5 \cdot s_1 \tag{A.1}$$

where s_1 is taken as the pedestal value. The value of S_5 depends only on the input charge Q. A correlation is also observed between Q and the partial integral S_4 and S_3 calculated as:

$$S_4 = S_5 - m_1; \qquad S_3 = S_4 - m_2 \tag{A.2}$$

where m_i are the single samples ordered by decreasing amplitude. The correlation between S_5 (S_4) and Q changes when one (two) of the samples saturate

as it can be seen in Fig. A.8, left. Each partial sum (S_i) corresponds to a fixed percentage of S_5 and thus there is a correlation between Q and S_4, S_3 and S_2.

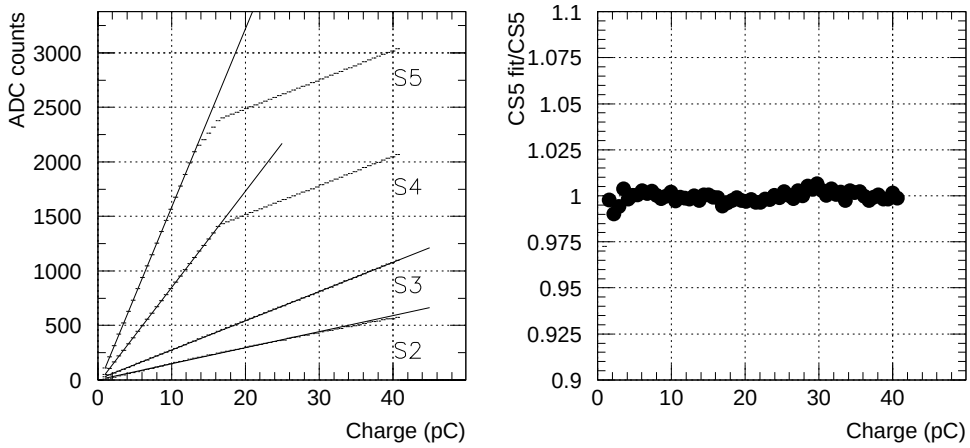

Fig. A.8. Left: mean value of the partial sums S_i, as defined in the text, as a function of the injected charge. The injected charge dependence of each S_i changes as soon as one or more time samples saturate. The linear fit is superimposed on each partial sum. Right: the linearity of the recovered signal is within 1 %.

The dependence of the mean value of S_i on Q is fit with a two parameter linear fit (Fig. A.8, left). Using these parameters we calculate the corrected integral signal of five samples $CS_5(S_4)$ ($CS_5(S_3)$) obtained from S_4 (S_3) when one (two) samples saturate. Applying this simple method in the high gain events allows us to extend the linearity region by more than a factor of three. The linearity of the recovered signal is shown in Fig. A.8 (right) – it is within 1 %.

A.3.2 Saturation Recovery Applied to Physics Events

The above described algorithm based on the flat filter was also used to study the saturation recovery on physics events. Electrons were chosen for this purpose. In the analysis, the saturation was simulated by neglecting the highest, or the two highest samples.

The values of S_4 and S_3 depend on the time difference between the trigger and the arrival of the first sampling (ΔT). The dependence of S_4/S_5 and S_3/S_5 on ΔT is calculated from the measured time shape of the signal and is used to evaluate $CS_5(S_4)$ and $CS_5(S_3)$ respectively. To demonstrate the linearity and resolution, the following quantities are defined:

$$\Delta S_5(S_i) = \frac{CS_5(S_i) - S_5}{S_5}, \qquad i = 3, 4 \tag{A.3}$$

As shown in Fig. A.9, the difference between the $CS_5(S_i)$ and S_5 is 0.4 % using

S_4 and 1 % using S_3. The obtained precision is 2 % with S_4 and 4.6 % using S_3. In terms of energy this means that, for a single cell, with a saturated sample in both channels, energies up to 1.9 TeV can be reconstructed with a loss of linearity of 0.4 %, while with two saturated samples up to 3.8 TeV can be reconstructed within the 1 %.

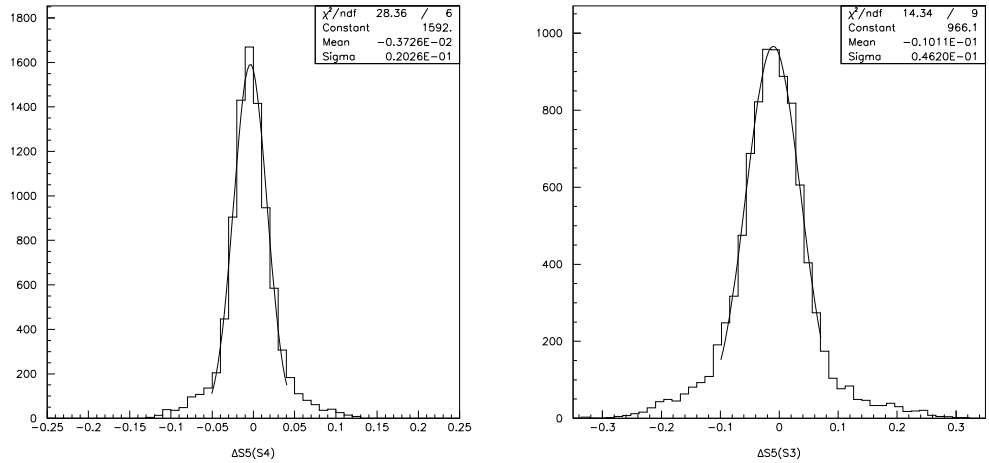

Fig. A.9. Distributions of $\Delta S_5(S_4)$ (left) and of $\Delta S_5(S_3)$ (right) for two saturated channels using electron data.

References

[1] G. Aad, et al., The ATLAS Experiment at the CERN Large Hadron Collider, JINST 3:S08003, 2008.

[2] ATLAS Collaboration, Expected Performance of the ATLAS Experiment – Detector, Trigger and Physics, CERN-OPEN-2008-020.

[3] ATLAS Collaboration, ATLAS Tile Calorimeter Technical Design Report, CERN/LHCC/96-42 (1996).

[4] J. Abdallah, et al., The Production and Qualification of Scintillator Tiles for the ATLAS Hadronic Calorimeter, ATLAS note ATL-TILECAL-PUB-2007-010.

[5] K. J. Anderson, et al., Nucl. Instr. and Meth. A 551 (2005) 469.

[6] S. Berglund, et al., The ATLAS Tile Calorimeter Digitizer, Proceedings of the 5th Workshop on Electronics for the LHC Experiments (LEB99), Snowmass, Colorado, USA, 1999; CERN/LHCC/99-33, 255-259.

[7] R. Teuscher, Methods of energy reconstruction in Tilecal, talk at Tilecal MC+Tools meeting (http://indico.cern.ch/conferenceDisplay.py?confId=a031558), 23.6.2003, CERN, Geneva.

[8] E. Fullana, Energy reconstruction algorithms and their influence on the ATLAS Tile Calorimeter, *Proceedings of the XI International Conference on Calorimetry in High Energy Physics* (Perugia, 2004).

[9] F. Sarri, Saturation recovery, talk at Tilecal MC+Tools meeting (http://indico.cern.ch/conferenceDisplay.py?confId=a031558), 23.6.2003, CERN, Geneva.

[10] W.E. Cleland, E.G. Stern, Nucl. Instr. and Meth. A 338 (1994) 467.

[11] R. Chadelas, et al., High voltage distributor system for the Tile hadron calorimeter of the ATLAS detector, ATLAS note ATL-TILECAL-2000-003.

[12] P. Bonneau, P. Grenier, A.M. Henriques-Correia, G. Montarou, G. Schlager, F. Varela-Rodriguez, M. Vassent, Performance and tests of the cooling system for the ATLAS Tile hadron calorimeter modules calibrations, ATLAS note ATL-TILECAL-2001-006.

[13] A.M. Henriques-Correia, A. Karioukhine, G. Schlager, Further performance tests of the cooling system for the calibration of the ATLAS Tilecal modules, ATLAS note, ATL-TILECAL-2002-014.

[14] N. Bouhemaid et al., Characterization of the Hamamatsu 10-stages R5900 photomultipliers at Clermont for the TILE calorimeter, ATLAS note ATL-TILECAL-97-108.

[15] K. J. Anderson, et al., Performance and Calibration of the TileCal Fast Readout Using the Charge Injection System, ATLAS note ATL-TILECAL-INT-2008-002.

[16] P. Grenier, et al., Analysis of the 1997 test beam laser data of the Tilecal extended barrel module 0, ATLAS note ATL-TILECAL-98-159.

[17] I. E. Chirikov-Zorin, et al., Nucl. Instr. and Meth. A 461 (2001) 587.

[18] X. Portell, et al., Distributions of Minimum Bias Current measurements in TileCal, ATLAS note ATL-TILECAL-2003-010.

[19] E. Starchenko, et al., Nucl. Instr. and Meth. A 494 (2002) 381.

[20] N. Shalanda, et al., Nucl. Instr. and Meth. A 508 (2003) 276.

[21] S. Errede, et al., The Effect of Tile Light Collection Reduction along Radius on the ATLAS Tile Calorimeter Uniformity, ATLAS note ATL-COM-TILECAL-2008-014.

[22] S. Agostinelli, et al., Nucl. Instr. and Meth. A 506 (2003) 250.

[23] J. Allison, et al., IEEE Trans. Nucl. Science, Vol. 53, No. 1 (2006) 270.

[24] Z. Ajaltouni, et al., Nucl. Instr. and Meth. A 388 (1997) 64.

[25] A. Bernstein, et al., Nucl. Instr. and Meth. A 336 (1993) 23.

[26] J. Proudfoot, R. Stanek, An Optical Model for the Prototype Module Performance from Bench Measurements of Components and the Test Module Response to Muons, ATLAS note ATL-TILECAL-95-066.

[27] J. Proudfoot, Light yield in the extended barrel prototype modules from electrons at 90 degrees, ATLAS note ATL-TILECAL-97-133.

[28] S. Nemecek, T. Davidek, R. Leitner, Light Yield Measurement of the 1998 Tile Barrel Module 0 using muon beams, ATLAS note ATL-TILECAL-99-003.

[29] J. G. Saraiva, S. Nemecek, A. Maio, Light yield Studies of the ATLAS Tile Calorimeter, ATL-TILECAL-PUB-2008-012.

[30] J. Abdallah, et al., The Optical Instrumentation of the ATLAS Tile Calorimeter, ATL-TILECAL-PUB-2008-005.

[31] R. Wigmans, *Calorimetry: Energy measurement in particle physics* (Clarendon Press, Oxford, 2000).

[32] A. Christov, Response of Production Modules of the ATLAS Tile Calorimeter to Electrons, ATLAS note ATL-TILECAL-PUB-2005-009.

[33] K. J. Anderson, et al., Calibration of ATLAS Tile Calorimeter at Electromagnetic Scale, ATLAS note ATL-TILECAL-PUB-2009-001.

[34] U. Blumenschein, I. Korolkov, M. Volpi, Calibration Constants for Integrators and Minimum Bias Monitoring, talk given at Tilecal Calibration Workshop (http://indico.cern.ch/conferenceDisplay.py?confId=23070), 12.11.2007, CERN, Geneva.

[35] V. Giangiobbe, D. Calvet, Performance of the TileCal super-drawers from a global analysis of the MobiDICK tests, ATL-TILECAL-PUB-2008-007.

[36] R. Wigmans, Nucl. Instr. and Meth. A 259 (1987) 389.

[37] J. Del Peso, E. Ros, Nucl. Instr. and Meth. A 295 (1990) 330.

[38] E. Bergeås, S. Hellman, K. Jon-And, Very Low Energy Muons in ATLAS TileCal, ATLAS note ATL-TILECAL-PUB-2005-001.

[39] M. Simonyan, Electron-pion separation in the ATLAS Tile hadron calorimeter, ATLAS note ATL-TILECAL-PUB-2006-003.

[40] H. Hakobyan, et al., Measurement of pion and proton longitudinal shower profiles up to 20 nuclear interaction lengths with the ATLAS Tile calorimeter, ATLAS note ATL-TILECAL-PUB-2007-008.

[41] M. Volpi, M. Cavalli-Sforza, Reanalysis of the Response of 95 Prototype Modules, ATLAS note ATL-COM-TILECAL-2008-019.

[42] T. A. Gabriel, et al., Nucl. Instr. and Meth. A 338 (1994) 336.

[43] D. E. Groom, Nucl. Instr. and Meth. A 572 (2007) 633.

[44] P. Amaral, et al., Nucl. Instr. and Meth. A 443 (2000) 51.

[45] T. Davidek, M. Volpi, T. Zenis, Response of the ATLAS Tile Calorimeter to Hadrons in Stand-Alone Testbeam Data, ATLAS note ATL-TILECAL-PUB-2009-004.

[46] S. Constantinescu et al., Comparative Analysis of the ATLAS Tile Calorimeter response to Pions and Protons, ATLAS note ATL-TILECAL-2001-005.

[47] P. Amaral, et al., Eur. Phys. J. C 20 (2001) 487.

[48] C. Alexa, et al., Eur. Phys. J. C 28 (2003) 297.

[49] S. Akhmadaliev, et al., Nucl. Instr. and Meth. A 480 (2002) 508.

[50] A. S. Cerqueira, T. Davidek, G. Usai, Tile Calorimeter Muon Trigger Signal, ATLAS note ATL-TILECAL-2002-002.

[51] A. S. Cerqueira, T. Davidek, Tilecal Trigger Signal Specifications and Testbeam Performance, ATLAS note ATL-TILECAL-PUB-2006-001.

[52] T. Del Prete, I. Vivarelli, The Timing of the Tile Calorimeter using laser events, ATLAS note ATL-TILECAL-2003-009.

[53] R. Leitner, V. V. Shmakova, P. Tas, Time resolution of the Atlas Tile calorimeter and its performance for a measurement of heavy stable particles, ATLAS note ATL-TILECAL-PUB-2007-002.

[54] C. Bohm, et al., ATLAS Tilecal Timing, ATLAS note ATL-TILECAL-2004-008.

[55] C. Roda, A study to assess the possibility to enlarge the Tile Calorimeter ADC dynamic range, ATLAS note ATL-TILECAL-2002-001.

[56] C. Roda, F. Sarri, Reconstruction of the time shape of the TileCal Signals, ATLAS note ATL-TILECAL-2003-007.